Oxidative Removal of Volatile Organic Compounds over the Supported Bimetallic Catalysts

Zhiquan Hou, Wenbo Pei, Xing Zhang, Yuxi Liu, Jiguang Deng and Hongxing Dai*

Beijing Key Laboratory for Green Catalysis and Separation, Key Laboratory of Beijing on Regional Air Pollution Control, Key Laboratory of Advanced Functional Materials, Education Ministry of China, Laboratory of Catalysis Chemistry and Nanoscience, Department of Chemistry and Chemical Engineering, College of Environmental and Energy Engineering, Beijing University of Technology, Beijing 100124, China

Abstract: Volatile organic compounds (VOCs) and methane are pollutants that are harmful to the atmosphere and human health. It is highly required to control emissions of VOCs. Catalytic oxidation is one of the most effective pathways for the elimination of VOCs, in which the key issue is the development of novel and high-performance catalysts. In this review article, we briefly summarize the preparation strategies, physicochemical properties, catalytic activities, and stability for the oxidative removal of VOCs of the supported bimetallic catalysts that have been investigated by our group and other researchers. The supported bimetallic catalysts include the supported noble bimetal, supported noble metal–transition metal, and supported non-precious bimetal catalysts. It was found that catalytic performance was related to one or several factors, such as specific surface area, pore structure, particle size and dispersion, adsorbed oxygen species concentration, reducibility, lattice oxygen mobility, acidity, reactant activation ability, and/or interaction between bimetals or between metal and support. The stability and ability of anti-poisoning to water, carbon dioxide or chlorine were related to the nature of the bimetal and support in the catalysts. In addition, we also envision the development trend of such a topic in the future work.

Keywords: Volatile organic compound, Oxidative removal, Supported noble bimetallic catalyst, Supported noble metal–transition metal or rare-earth catalyst, Supported non-precious bimetal catalyst.

1. INTRODUCTION

Volatile organic compounds (VOCs) or chlorinated organic compounds (CVOCs) are one class of the main air pollutants [1,2]. Most of the VOCs and CVOCs are emitted from motor vehicles, shipbuilding, painting, printing, pharmaceuticals, rubber and plastics processing, kitchen fume, chemical industries [3,4], and combustion systems [5–7], which include light hydrocarbons, aromatics, alcohols, ketones, ethers, esters, aldehydes, carboxylic acids, amines, and halogen- or sulfur-containing organics [1,8]. Most of VOCs and CVOCs are proven to be toxic, malodorous, flammable or even explosive [9]. Hence, it is highly required to control the emissions of VOCs and CVOCs. Up to now, the main pathways for VOCs and CVOCs removal are physical (adsorption, absorption, and membrane separation) and chemical (catalytic oxidation, incineration, plasma destruction, and photocatalysis) methods. It is well known that catalytic oxidation is thought to be the most effective pathway, in which the critical issue is the development of high-performance catalysts [10]. So far, the catalysts used for VOCs and CVOCs oxidation include single or mixed transition metal oxides, rare-earth oxides, and their supported noble metals [3,11]. It has been shown that the single or mixed transition metal oxides and rare-earth oxides are low cost but show low activities at low temperatures, while the supported noble metals are expensive but exhibit good low-temperature catalytic performance [10,11]. Among the supported noble metal catalysts, the supported bimetallic catalysts have been particularly gaining much attention since they perform well at low temperatures and show good performance towards the poisoning of water, carbon dioxide, and chlorine or sulfur. In the past years, some researchers have summarized the research progress on preparation and catalytic activities of the catalysts developed to date for VOCs removal [4,8,10].

In this review article, we briefly summarize the preparation strategies, physicochemical properties, and catalytic activities for the oxidative removal of VOCs and CVOCs of the supported bimetallic catalysts that have been investigated by our group and other researchers [12–77]. The supported bimetallic catalysts are classified into three categories: supported noble bimetal catalysts, supported noble metal–transition metal or rare-earth catalysts, and supported non-precious bimetal catalysts. Bimetallic catalysts have applications in many fields, such as electrocatalysis, photocatalysis, and even sensors. This article mainly reviews their applications in the oxidation of VOCs and

*Address correspondence to this author at the Department of Chemistry and Chemical Engineering, College of Environmental and Energy Engineering, Beijing University of Technology, Beijing 100124, China; Tel: +8610-6739-6118; Fax: +8610-6739-1983; E-mail: hxdai@bjut.edu.cn

E-ISSN: 2410-3624/20

Table 1: Reaction Conditions, Catalytic Activities, and Specific Reaction Rates of the Catalysts Reported in the Literature

Catalyst	Reactant concentration	SV (mL/(g h))	Activity ($T_{90\%}$)	Specific reaction rate (μmol/(g s))/ (temperature (°C))	Ref.
$1.81Pd_{2.1}Pt/6.70MnO_x$/3DOM $CoFe_2O_4$	2.5 vol% methane	20,000	372	75.3[a]/250	[12]
$1.41Pd_{5.1}Pt$/meso-Mn_2O_3	2.5 vol% CH_4	20,000	425	6.39[b]/400	[14]
PdPt@SiO_2	4000 ppm CH_4	133,800	420	2.353[b]/420	[15]
Au_3Pd_7/TiO_2	1000 ppm CO	48,000	129 ($T_{50\%}$)	0.364[b]/200	[16]
$1.93AuPd_{1.95}$/3DOM $CoCr_2O_4$	2.5 vol% CH_4	20,000	394	1.15[b]/320	[17]
$1.91AuPd_{1.80}$/3DOM $LaMnAl_{11}O_{19}$	2.5 vol% CH_4	20,000	402	0.74[b]/310	[18]
$1.95Au_1Pd_2$/meso-Cr_2O_3	1000 ppm toluene	20,000	165	0.091[b]/120	[21]
0.96($AuPd_{1.92}$)/Co_3O_4	1000 ppm toluene 1000 ppm *o*-xylene	40,000 40,000	180 187	0.269[b]/180 0.264[b]/187	[22]
Au_1Pd_2/CZY	1000 ppm toluene	20,000	218	47.8[a]/220	[23]
Au–Pd–0.21Co/3DOM Mn_2O_3	2.5 vol% CH_4	40,000	213	6.269[b]/213	[24]
$0.68Ag_{0.75}Au_{1.14}Pd$/meso-Co_3O_4	1000 ppm toluene	80,000	112	0.633[b]/112	[25]
1AuPd/3DOM LSMO	2.5 vol% CH_4	40,000	335	3.63[b]/270	[27]
Pt_xAg_{1-x}/HZ-S	120 ppm benzene	30,000	115	0.028[b]/115	[28]
$3.8AuPd_{1.92}$/3DOM Mn_2O_3	1000 ppm toluene	40,000	162	10.5[a]/162	[32]
1.99AuPd/3DOM Co_3O_4	1000 ppm toluene	40,000	168	21.43[a]/170	[33]
$2.85AuPd_{1.87}$/3DOM CeO_2	750 ppm trichloroethylene	20,000	415	11.8[a]/300	[34]
$2.05Au/0.70FeO_x/CeO_2$	1400 ppm toluene	32,000	300	45.9[b]/300	[35]
1.00Au/6CoO/SiO_2-2	1.0 vol% CO	12,000	167	12.1[a]/187	[36]
1.21Au–8.50Co-10/UVM-7	1000 ppm propane	20,000	320	–	[34]
AuCo-10/UVM-7	1000 ppm toluene	20,000	275	12.3[a]/275	[37]
$5.10Au/MnO_x/Al_2O_3$	0.5 vol% methane	30,000	580	39.6[a]/580	[38]
$0.93Au/11.2MnO_x$/3DOM SiO_2	1000 ppm toluene	20,000	255	9.5[a]/255	[39]
$1.67Mn_3O_4$–2.00Au/3DOM LSCO	1000 ppm toluene	20,000	230	20.5[a]/230	[40]
1.00Pd@CeO_2/Si–Al_2O_3	0.5 vol% methane	20,000	390	66.7[a]/320	[41]
1.00Pd@ZrO_2/Si–Al_2O_3	1.0 vol% methane	18,000	400	120.1[a]/320	[42]
0.50Pd–Co/ Al_2O_3	0.4 vol% methane	50,000	520	128.7[a]/430	[43]
0.20Pd/Co–Ce (6 : 1)/Al_2O_3	1000 ppm benzene	20,000	185	86.6[a]/140	[44]
$0.26Pd@CoO_x$/3DOM CeO_2	2.5 vol% methane	40,000	480	1334.3[a]/440	[45]
$1.37Pd–GaO_x/Al_2O_3$	0.5 vol% methane	80,000	372	23.32[a]/290	[46]
1.10Pd/Al_2O_3–36NiO	1.0 vol% methane	48,000	460	126.1[a]/310	[47]
0.40Pd/0.50NiO/Al_2O_3	1.0 vol% methane	30,000	350	112.5[a]/255	[48]
0.80Pd/10.00V_2O_5/Al_2O_3	482 ppm benzene	30,000	257	38.4[a]/257	[49]
Au–Pd–0.40CoO/3DOM Co_3O_4	2.5 vol% methane	20,000	341	88.0[a]/280	[50]
0.25Pt/23CeO_2–Al_2O_3	1000 ppm *n*-butanol	60,000	167	54.7[a]/70	[51]
$10.0Pt/16.0Ce_{0.64}Zr_{0.16}Ni_{0.2}O_{1.9}/Al_2O_3$	1000 ppm toluene	12,000	100 ($T_{100\%}$)	1.36[a]/100	[52]
$0.02Pt_1–Co_3O_4$	700 ppm methanol	30,000	96	1.3×10^{5}[a]/70	[53]
0.50Pt–15Co/RH-MCM-41	1974 ppm ethanol	9,550	285	77.3[a]/285	[54]
1.30Pt/8.90Co_3O_4/3DOM Al_2O_3	1000 ppm toluene	20,000	160	28.2[a]/160	[55]

(Table 1) contd….

$Pt_{0.3}Mn_5/SiO_2$-nc	800 ppm MEK	42,600	147	32.9[a]/100	[56]
$0.31Pt–WO_3/Ce_{0.65}Zr_{0.35}O_2$	1000 ppm toluene	12,000	220 ($T_{100\%}$)	43.9[a]/220	[57]
16.9 wt% CuO–12.5 wt% CeO_2/USY	1000 ppm 1,2-dichloroethane	15,000	288	0.63[b]/265	[58]
17.5 wt% Cr_2O_3–12.5 wt% CeO_2/USY	1000 ppm trichloroethylene	15,000	281	0.77[b]/265	[59]
1.5 wt% $Cr_{1.0}Cu_{0.5}/SiCl_4$-Z	2500 ppm trichloromethane	32,000	300	0.8[b]/275	[60]
40 wt% $(Ce,Cr)_xO_2$/HZSM-5	1000 ppm 1,2-dichloroethane	9,000	230	0.31[b]/210	[61]
8 wt% Cr_6Ce_1/Al_2O_3/Ti-PILC	1000 ppm *n*-butylamine	20,000	220	0.53[b]/190	[62]
2 wt% MnCe(9 : 1)/AlZr-PILC	1000 ppm chlorobenzene	20,000	263	0.45[b]/250	[63]
10 wt% CrCe(6 : 1)/Ti-PILC	500 ppm chlorobenzene	20,000	210	0.39[b]/200	[64]
20 wt% Mn_4Ce_1/cordierite	500 ppm chlorobenzene	15,000	364	0.16[b]/320	[65]
9 wt% Cr–12 wt% CeO_2/HZSM-5	1000 ppm trichloroethylene	15,000	269	0.52[b]/240	[66]
20 wt% $Mn_{0.8}Ce_{0.2}O_2$/H-ZSM5	1000 ppm chlorobenzene	10,000	230	0.16[b]/210	[67]
46 wt% Cu–Mn(1:6)/ZSM-5/PSSF	4.7 mg/L isopropanol	3,822	210	0.79[b]/300	[68]
10 wt% Ni–Mn/cordierite	1000 ppm toluene	10,000	300	0.59[b]/250	[69]
Cu_1Mn_2/Fe-Sep	2000 ppm ethyl acetate	20,000	210	0.19[b]/180	[70]
4.4 wt% MnCe(2/1)/Al-MSPs	1000 ppm acetone	15,000	135	1.5[b]/125	[71]
15 wt% Mn_8Ce_2/Al_2O_3	1000 ppm chlorobenzene	15,000	315	0.8[b]/290	[72]
3 wt% $Mn_4–Ce_1/Al_2O_3$	1000 ppm chlorobenzene	15,000	370	0.79[b]/260	[73]
10 wt% $CuMn(1)O_x/\gamma$-Al_2O_3	1200 ppm toluene	15,000	229	0.31[b]/210	[74]
5 wt% $MnCuO_x/TiO_2$	500 ppm chlorobenzene	5,000	318	0.16[b]/285	[75]
5 wt% Cu_2Mn_1/Zr–Ti–Al	1200 ppm dichloromethane	15,600	455	0.32[b]/430	[76]
40 wt% $(Ce,Cr)_xO_2/Nb_2O_5$	1000 ppm 1,2-dichloroethane	9,000	253	0.31[b]/250	[77]

Note: [a] The specific reaction rate (μmol/($g_{Noble\ metal}$ s)); and [b] the specific reaction rate (μmol/(g_{cat} s)).

CVOCs. We use the reaction temperature ($T_{x\%}$) at which the conversion of a VOC or CVOC reached a certain level (for example, 10, 50, 90 or 100%) at a given space velocity (SV) to compare activities of different catalysts. Since the reaction temperature over a catalyst usually increases with a rise in SV, the specific reaction rate at a certain reaction temperature is also employed to evaluate the catalytic activity. Table **1** summarizes the reaction conditions, catalytic activities, and specific reaction rates of the catalysts reported in the literature.

2. SUPPORTED NOBLE BIMETAL CATALYSTS

Bimetal in a catalyst can regulate the electronic state of the catalyst surface due to the interaction between the two metals, which renders the bimetallic catalysts to show better activity than the single metal catalysts. Two noble metals among bimetallic alloys have different electronic and crystal structures (hence different surface characteristics), which make bimetallic catalysts perform differently, as compared with their single metal counterparts. These differences are often manifested in activity, stability, and water-, carbon dioxide-, and halogen-resistance. Such conclusions have been confirmed by a number of works on the catalysts, such as $1.81Pd_{2.1}Pt/6.70MnO_x$/3DOM $CoFe_2O_4$ [12], PdPt–Y–ZrO_2 [13], and $1.41Pd_{5.1}Pt$/meso-Mn_2O_3 [14]. For instance, Habibi *et al.* [15] adopted a Stöber-based method to prepare the PdPt high-loading silica-encapsulated (PdPt@SiO_2 with 4 wt% Pd and 7 wt% Pt) catalysts, and investigated their catalytic behaviors in lean methane combustion in the presence of water up to 550 °C (Figure **1**). The as-synthesized bimetallic core particles displayed an average size of 7 nm, and the formed uniform PdPt alloys were well dispersed inside the oxide shells. The catalyst showed an enhanced activity ($T_{90\%}$ = 420 °C at 4000 ppm CH_4 and 5 mol% H_2O) and a stable methane conversion in the hydrothermal ageing (HTA) test which was two- and ten-fold higher than methane conversions over the impregnated Al_2O_3 and SiO_2-supported catalysts at the same metal loading, respectively.

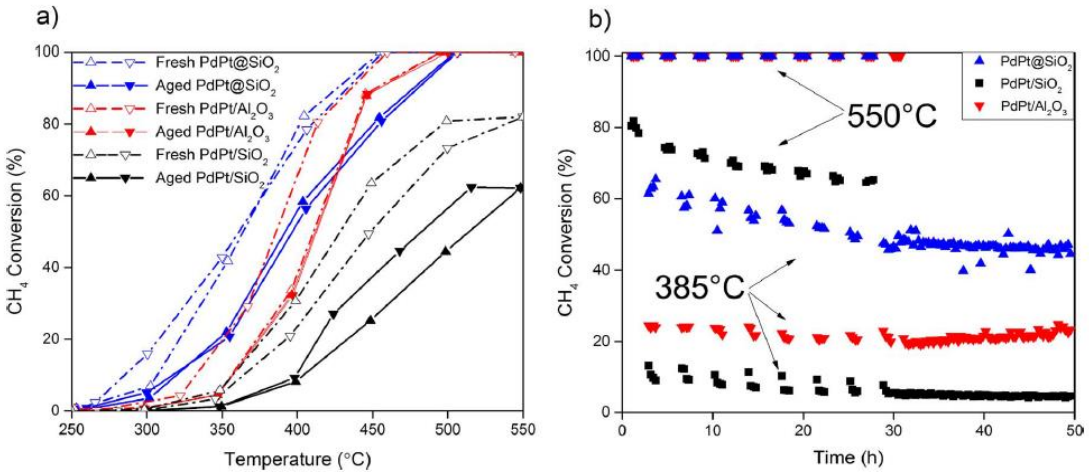

Figure 1: (**a**) Ignition (pyramid symbols) and extinction (inverted pyramids) data before and after HTA; (**b**) methane conversion versus time on stream during HTA. Reaction conditions: 100 mg catalyst (4.205 wt% Pd, 6.98 wt% Pt), space velocity (SV) = 133,800 $L_{STP}/(kg_{cat}\ h)$, initial CH_4 concentration 4000 ppm and 5 mol% H_2O [15].

Besides, the other noble bimetal or even trimetal catalysts also exhibited enhanced performance for VOCs oxidation. For example, Tofighi *et al.* [16] prepared the Au_xPd_y NPs (1 nm in size) with different Au/Pd ratios in a continuous microfluidic reactor, then deposited them on the surface of TiO_2, and explored the active sites of the monometallic Au and Pd NPs and bimetallic Au_xPd_y nanoalloys using the temperature-dependent IR spectroscopy with CO as a probe molecule. The results demonstrated the presence of strong electronic interactions between Au and Pd in the alloyed bimetals, leading to an interatomic charge transfer and electronic modifications in the *d* bands of Au and Pd. The $AuPd/TiO_2$ sample with an Au/Pd ratio of 3 : 7 exhibited the highest catalytic activity ($T_{50\%}$ = 129 °C at SV = 48,000 h^{-1}) in CO oxidation, as compared with the other alloy samples (Figure **2**). This was attributed to a synergistic effect, which facilitated the activation of dioxygen at the Pd-enriched sites, while both bimetallic Au and Pd sites chemisorbed CO molecules. Similar cases also appeared in methane catalytic combustion. Three-dimensionally ordered macroporous (3DOM) $CoCr_2O_4$-supported Au–Pd alloy (xAuPd$_y$/3DOM $CoCr_2O_4$; x = 0.98 and 1.93 wt%, and Pd/Au molar ratio (y) = 1.93–1.96) nanocatalysts [17] derived from the polyvinyl alcohol-protected reduction route performed good performance for methane combustion. The $1.93AuPd_{1.95}$/3DOM $CoCr_2O_4$ sample showed the best catalytic activity with the $T_{10\%}$, $T_{50\%}$, and $T_{90\%}$ being 305, 353, and 394 °C at a SV of 20,000 mL/(g h), respectively. Similar results were also obtained by the other researchers [18–20].

Dai and coworkers [21] prepared the three-dimensionally ordered mesoporous Cr_2O_3 (meso-Cr_2O_3) and its supported Au, Pd, and AuPd (0.90 wt% Au/meso-Cr_2O_3, 1.00 wt% Pd/meso-Cr_2O_3, and xAu$_1$Pd$_2$/meso-Cr_2O_3 (x = 0.50–1.95 wt%) catalysts

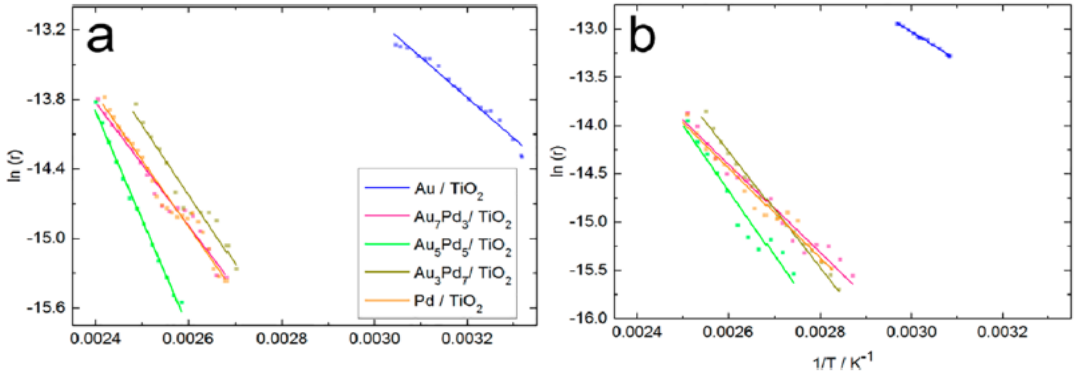

Figure 2: Arrhenius plots for CO oxidation over the Au/TiO_2, Au_3Pd_7/TiO_2, Au_5Pd_5/TiO_2, Au_7Pd_3/TiO_2, and Pd/TiO_2 catalysts after (**a**) N_2 and (**b**) H_2 pretreatment. Conditions: 1000 ppm CO, 10 vol% O_2 in N_2 (balance), SV = 48000 h^{-1}, and ramp rate = 1 K/min [17].

using the KIT-6-templating and polyvinyl alcohol-protected reduction methods, respectively. It was found that the 1.95Au_1Pd_2/meso-Cr_2O_3 sample performed the best: the $T_{10\%}$, $T_{50\%}$, and $T_{90\%}$ were 87, 145, and 165 °C at a SV of 20,000 mL/(g h) (Figure **3**), respectively, and the apparent activation energy was the lowest (31 kJ/mol) among all of the samples. The authors concluded that the excellent catalytic performance of 1.95Au_1Pd_2/meso-Cr_2O_3 was associated with its small Au-Pd particle size, high adsorbed oxygen species concentration, good low-temperature reducibility, and strong interaction between AuPd NPs and meso-Cr_2O_3. Wang *et al.* [22] prepared Co_3O_4 octahedron-supported AuPd (xAuPd$_y$/Co_3O_4; x = 0.18, 0.47, and 0.96 wt%; y (Pd/Au molar ratio) = 1.85–1.97) nanocatalysts using the molten salt and polyvinyl alcohol-protected reduction methods, and observed good activities of these materials for the oxidative removal of toluene and *o*-xylene. In addition, the 0.90Au_1Pd_2/CZY [23] and 1.94 wt% Au–Pd–0.21Co/3DOM Mn_2O_3 [24] also performed well in the oxidation of VOCs.

Yang *et al.* [25] prepared the Ag_xAu_yPd/meso-Co_3O_4 catalysts by the polyvinyl alcohol-protected $NaBH_4$ reduction approach, and evaluated their catalytic performance for methanol combustion. They found that 0.68 wt% $Ag_{0.75}Au_{1.14}Pd$/meso-Co_3O_4 showed the highest catalytic activity ($T_{50\%}$ = 100 °C and $T_{90\%}$ = 112 °C at a SV of 80,000 mL/(g h) (Figure **4**). As shown in the HAADF–STEM images of the 0.68$Ag_{0.75}Au_{1.14}Pd$/meso-Co_3O_4 sample (Figure **5**), Ag, Au, Pd, and Ag_xAu_yPd NPs were uniformly dispersed on the surface of meso-Co_3O_4. The good catalytic performance of 0.68 wt% $Ag_{0.75}Au_{1.14}Pd$/meso-Co_3O_4 was related to the strong interaction between $Ag_{0.75}Au_{1.14}Pd$ alloy NPs and meso-Co_3O_4, high O_{ads} species concentration, and good low-temperature reducibility.

There are also many explorations on the reasons for the activity improvement of bimetallic catalysts. Saint-Lager *et al.* [26] studied the changes of AuPd particles during the reaction process. The evolution of the $Au_{30}Pd_{70}$(110) surface was examined by means of coupling grazing incidence X-ray diffraction and mass spectrometry under the oxygen-rich conditions at moderate temperatures (27 to 197 °C), so that the depth profile of the structure could correlate to its catalytic properties for carbon monoxide oxidation (Figure **6**). It was found that both oxygen and CO induce Pd segregation at an increasing pressure from ultrahigh vacuum up to 100 mbar. However, in pure oxygen, the surface was reorganized with a (1 × 2) missing row reconstruction, whereas in pure CO it was strongly roughened. When oxygen pressure was increased a phase corresponding to the initial step of the oxidation with oxygen dissolution in the subsurface

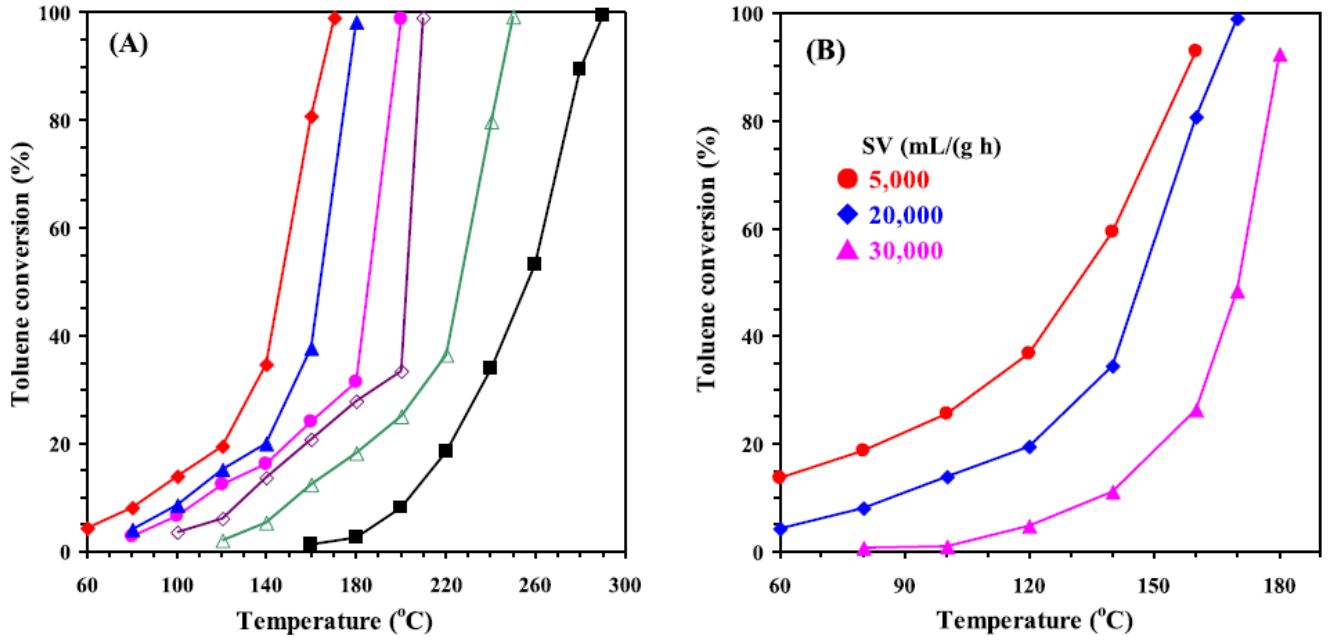

Figure 3: (**A**) Toluene conversion as a function of reaction temperature of the (■) meso-Cr_2O_3, (●) 0.50Au1Pd_2/meso-Cr_2O_3, (▲) 0.97Au_1Pd_2/meso-Cr_2O_3, (◆) 1.95Au_1Pd_2/meso-Cr_2O_3, (△) 0.90Au/meso-Cr_2O_3, and (◇) 1.00Pd/meso-Cr_2O_3 samples at SV = 20,000 mL/(g h), and (**B**) effect of SV on the catalytic activity of 1.95Au_1Pd_2/meso-Cr_2O_3 for toluene oxidation [21].

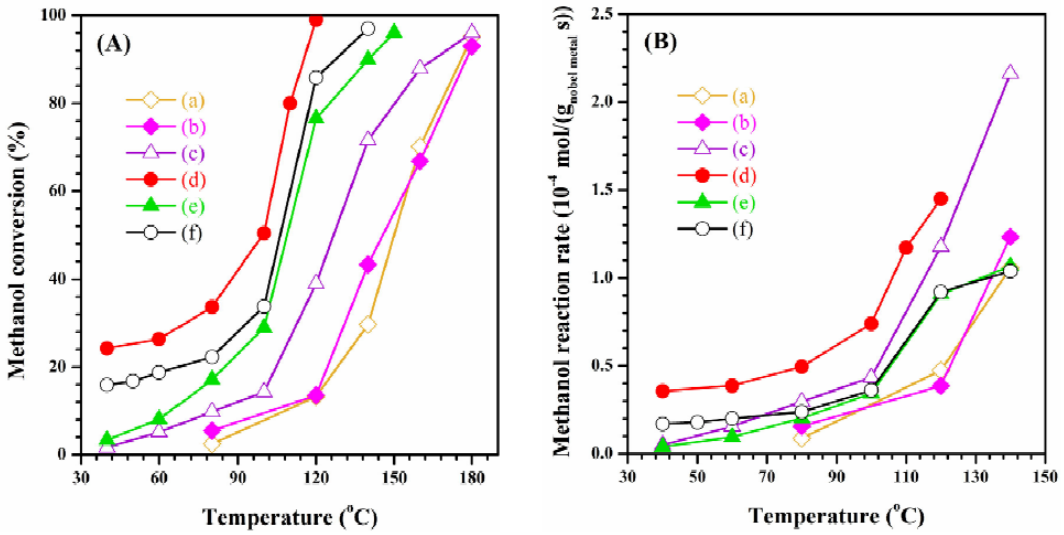

Figure 4: (**A**) Methanol conversion and (**B**) reaction rate normalized per gram of noble metal versus temperature over (**a**) 0.28Ag/meso-Co_3O_4, (**b**) 0.35Au/meso-Co_3O_4, (**c**) 0.33Pd/meso-Co_3O_4, (**d**) 0.68$Ag_{0.75}Au_{1.14}$Pd/meso-Co_3O_4, (**e**) 0.84$Ag_{0.54}Au_{2.29}$Pd/meso-Co_3O_4, and (**f**) 0.93$Ag_{0.51}Au_{0.65}$Pd/meso-Co_3O_4 [25].

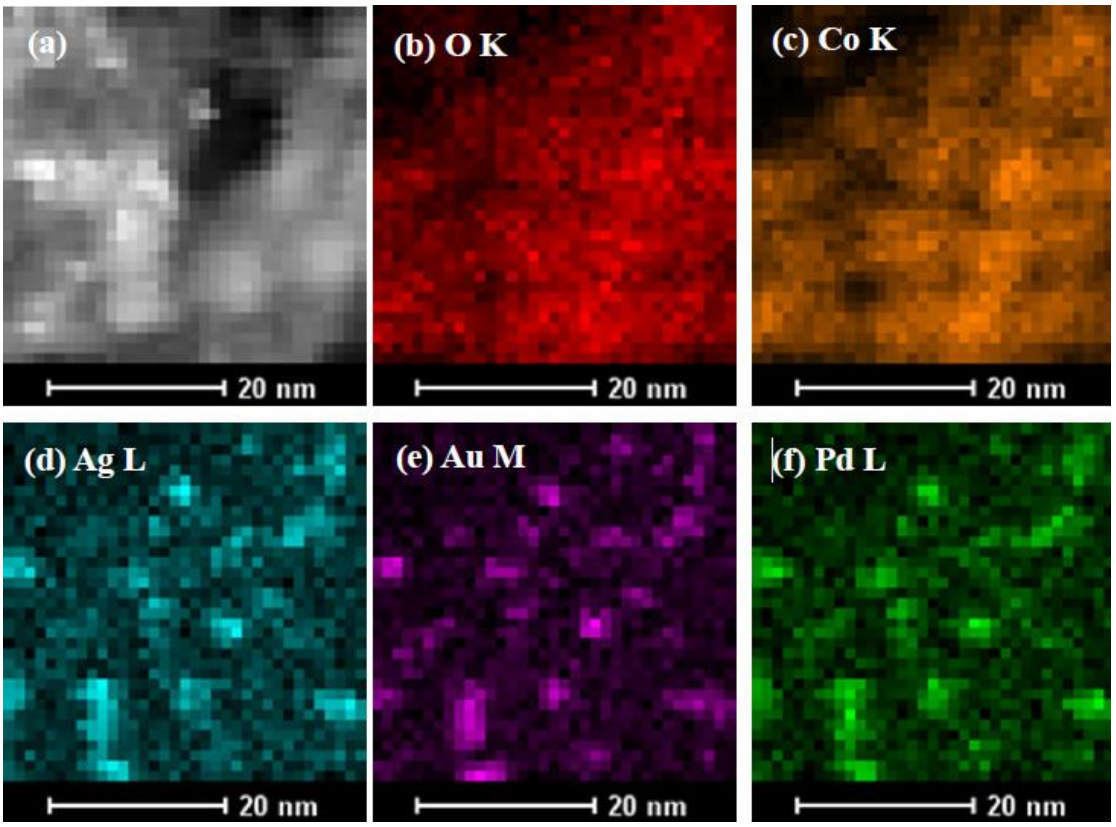

Figure 5: HAADF–STEM and elemental scanning images of the 0.68$Ag_{0.75}Au_{1.14}$Pd/meso-Co_3O_4 catalyst [25].

region appeared at first. Then, an oxidized thin Pd layer (≤ 1 nm) was formed from about 127 °C and grew in the PdO(100) direction. This PdO phase was strained and did not coincide with the *P*42/*mmc* structure usually observed for this oxide under ambient conditions. It might be more probably consistent with the high-pressure *I*4/*mmm* PdO structure strained by epitaxy on the underneath alloy. Under the higher oxidizing conditions and at higher layer thickness, the oxide was then relaxed to the usual PdO structure. This

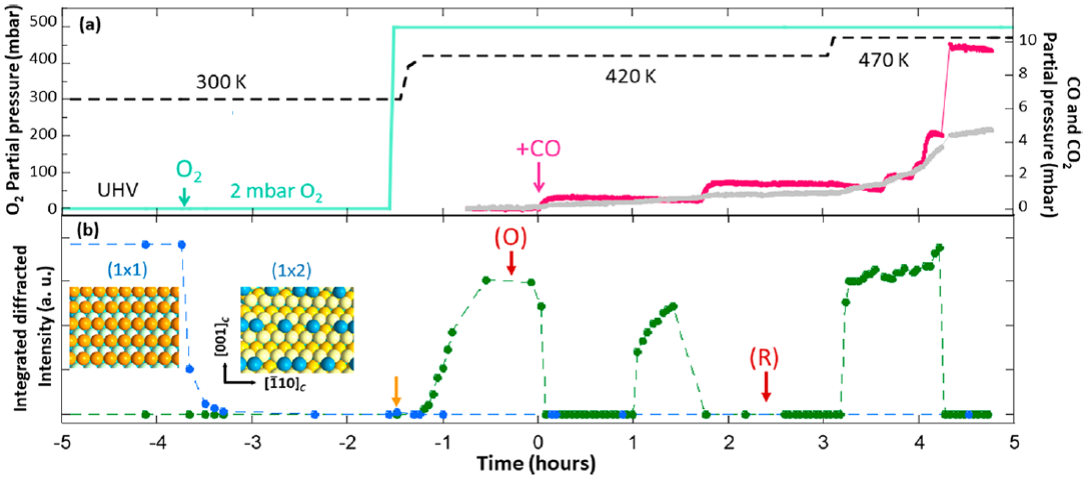

Figure 6: (a) Variation of partial pressures of oxygen (turquoise and left vertical axis), of CO and produced CO_2 (right vertical axis, pink and gray, respectively) over time. 2 mbar of oxygen was introduced at time = 3.75 h (small green vertical arrow) and the pressure was then increased to 500 mbar; the pink arrow indicates the first CO introduction (at time = 0 h), the following jumps in the CO pressure correspond to new CO additions. The black dashed line indicates the temperature level. (b) Variation induced on the integrated intensity of the (0 1 0.05) surface peak (in blue) and of the (0 1.47 0.05) oxide peak (in dark green) [≡(002)PdO Bragg peak], the dashed lines are guides for the eyes. The two insets are schematic representations of the (1 × 1) and (1 × 2) $Au_{30}Pd_{70}$(110) surfaces with the close-packed rows along $[1\ 1\ 0]_C$ [26].

strained oxide was easily reduced by CO and exhibited a high activity for CO oxidation, and the activity at 197 °C was comparable to that over the pure palladium at higher temperatures. Moreover, oxidation on the clean $Au_{30}Pd_{70}$(110) surface was inhibited up to 197 °C if CO was introduced prior to oxygen. This result indicated that when Pd was alloyed with gold, its binding with CO became stronger than that with oxygen. The weakening of the Pd−O binding by surrounding gold atoms was the key in generating a well-ordered and active thin PdO film on $Au_{30}Pd_{70}$(110).

For the enhanced performance, it would have different reaction pathways. Wang *et al.* [27] explored it using the *in situ* diffuse reflectance infrared Fourier transform infrared spectroscopy (*in situ* DRIFTS). Bimetallic Au−Pd alloy NPs dispersed on nanohybrid 3DOM-structured $La_{0.6}Sr_{0.4}MnO_3$ (LSMO) perovskite catalysts were fabricated via the L-lysine-mediated colloidal crystal-templating and reduction routes. The Au−Pd alloy presence favored the enhancement in catalytic activity for methane combustion. There were three advantages of the 3DOM LSMO support: (i) a large surface area (32−34 m^2/g) which was beneficial for the high dispersion of the noble metal NPs on the support surface; (ii) abundant Brønsted acid sites which could facilitate reactant adsorption and activation; and (iii) thermal stability. The former two factors contributed to provide enhanced activity and a structure with (hydro)thermal stability. For the AuPd alloy particles, the results of the *in situ* DRIFTS characterization (Figure **7**) revealed that inclusion of Au in the bimetallic system accelerated the reaction rate and altered the reaction pathway for methane oxidation by enriching the adsorbed oxygen species and decreasing the bonding strength between the reaction intermediates and the Pd atoms.

The crystal size of a support can influence the dispersion of active bimetal particles. Wang *et al.* [28] prepared the HZSM-5-supported bimetallic PtAg catalysts (Figure **8**), with the investigation being focused on HCHO oxidation at room temperature, benzene storage capacity at room temperature, and benzene oxidation at elevated temperatures. The HZSM-5 was denoted as HZ-L, HZ-M, and HZ-S in terms of its particle size (large, medium, and small), respectively. It was found that the crystal size of HZSM-5 not only influenced the dispersion of active PtAg (hence influencing their catalytic properties for formaldehyde and benzene oxidation (Figure **9**)), but also exerted considerable effects on benzene storage capacity and thermal stability of the stored benzene, which was directly related to the release of benzene at elevated temperatures. The Pt/Ag ratio showed an opposite effect on benzene storage capacity and formaldehyde or benzene oxidation properties. Therefore, the PtAg/HZSM-5 catalyst at a Pt/Ag ratio of 1/1 was suitable for the proposed cycling process, in which a good carbon balance was obtained in each cycle and no secondary pollutants were produced. However, reducibility of the support did not affect the

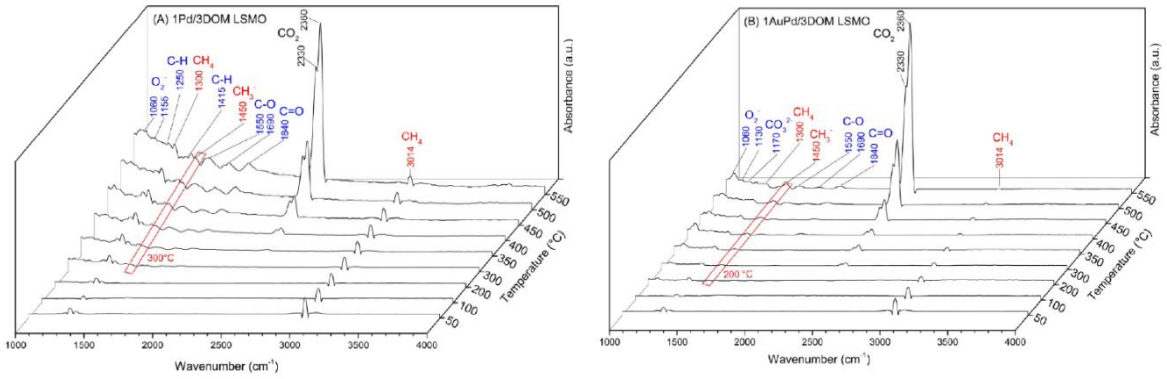

Figure 7: *In situ* DRIFTS spectra of methane oxidation over (**A**) 1Pd/3DOM LSMO and (**B**) 1AuPd/3DOM LSMO [27].

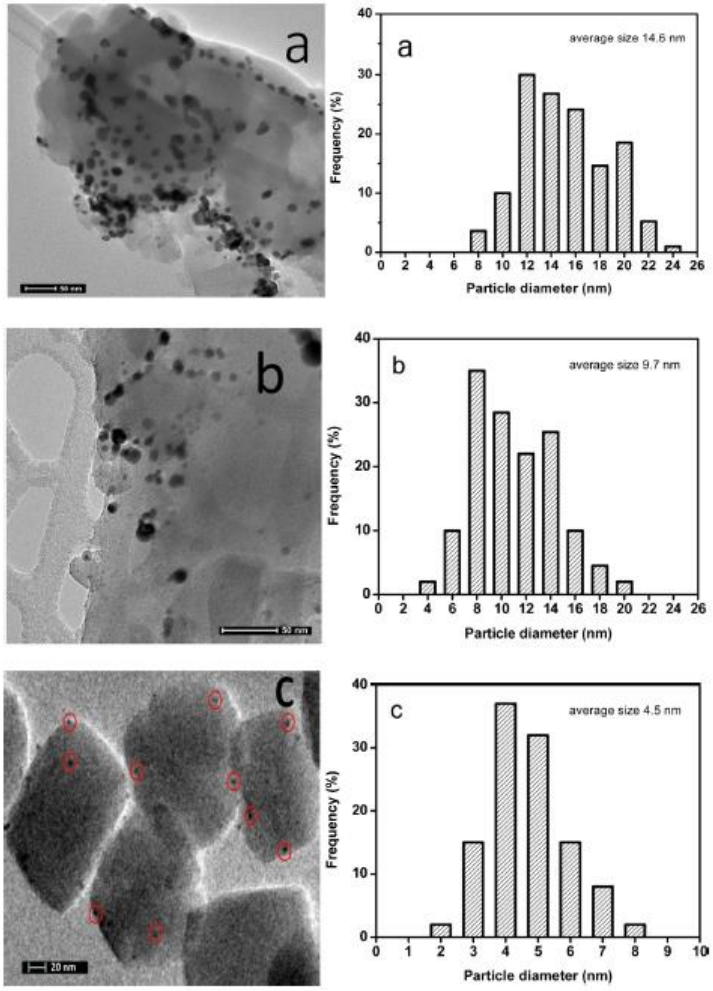

Figure 8: TEM images and particle size histograms of (**a**) $Pt_{0.5}Ag_{0.5}$/HZ-L, (**b**) $Pt_{0.5}Ag_{0.5}$/HZ-M, and (**c**) $Pt_{0.5}Ag_{0.5}$/HZ-S [28].

surface structure. Abbott *et al.* [29] employed the model systems (in which mono- and bimetallic Au–Pd NPs were deposited on the well-ordered thin films of reducible and irreducible oxides (*e.g.*, Fe_3O_4(111), MgO(100), and CeO_2(111)) to gain a deep understanding on the structure–reactivity relationship of the Au–Pd catalysts. Surface structures of the model systems were characterized by means of temperature-programmed desorption, sum-frequency generation, and infrared reflection absorption spectroscopy (IRAS) using CO as a probe molecule (Figure **10**). The results. showed segregation of gold to the surface, which was

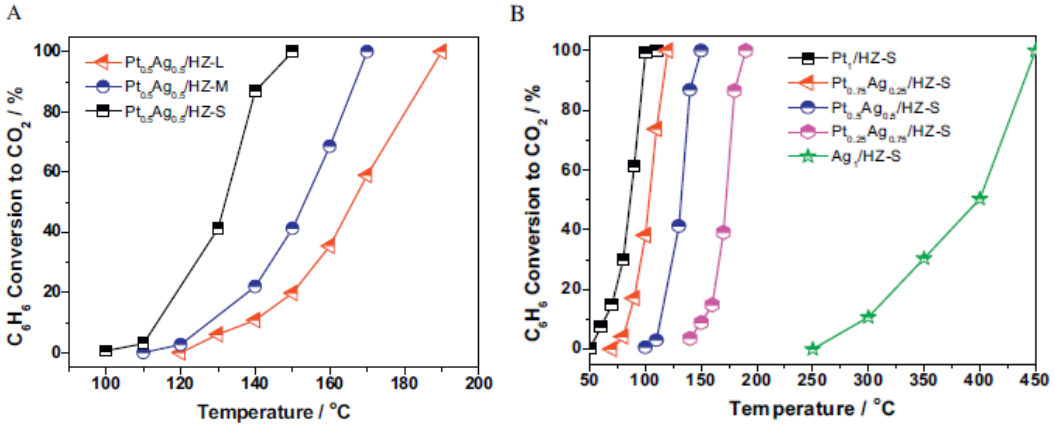

Figure 9: Complete oxidation of C_6H_6 to CO_2 over (**A**) $Pt_{0.5}Ag_{0.5}$/HZ-S (-M and -L) and (**B**) Pt_xAg_{1-x}/HZ-S [28].

confirmed by the results of density functional theory calculations that Au preferred to be at the edges of AuPd alloy particles under vacuum conditions. The strong similarities between the spectral features observed for metal particles on these oxide substrates suggested that reducibility of the support did not influence the surface structure

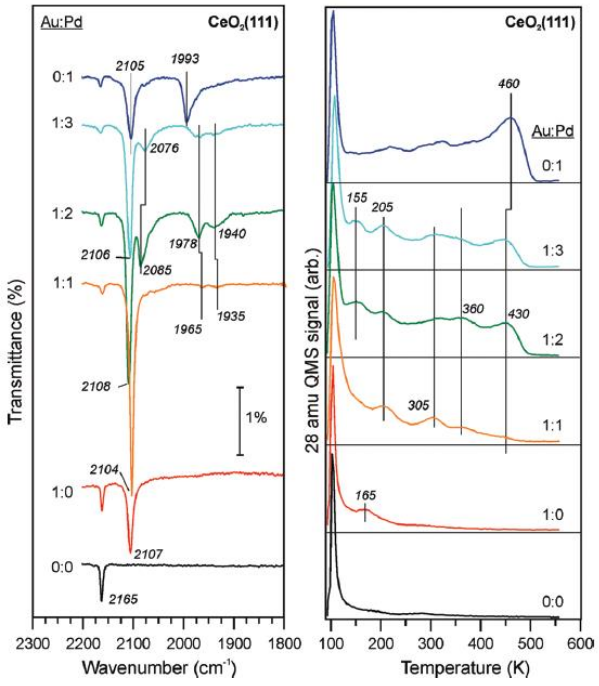

Figure 10: IRAS spectra (left) and TPD profiles (right) for 10 L CO adsorbed at *ca.* −173 ºC on the Pd, Au, and Au-Pd particles supported on the CeO_2(111) thin films. The particle composition was varied as indicated by the Au/Pd ratios with a nominal Pd thickness of *ca.* 1 Å. IRAS spectra were acquired at −173 ºC, and the heating rate in each TPD experiment was 5 K/s [29].

It has been reported that the catalysts loaded with Pt–Pd bimetals possessed high catalytic activities and good thermal stability for the combustion of organics [13,30]. Zhu and coworkers [30] prepared the monolithic Pt–Pd bimetallic catalysts supported on *γ*-Al_2O_3 with cordierite honeycomb ceramics as the first support by the thermal adsorption method. The as-prepared catalysts exhibited better performance than the commercial catalyst for the combustion of benzene and other aromatic hydrocarbons.

The addition of Pt could activate methane in an oxygen-deficient atmosphere, but water could exert an inhibitory effect on the support-mediated oxygen-exchanged PdPt bimetal catalysts for methane combustion. Hayes and coworkers [31] prepared a silica-encapsulated bimetallic Pd−Pt (1 : 1 in molar ratio) catalyst, and examined the effect of moisture on lean methane combustion over the catalysts at varying methane concentrations and temperatures in the absence or presence of water (Figure **11**). It was found that two rate equations were necessary to describe the kinetics: one for the case of dry feed and the other for the case of wet feed. Under the wet conditions, water suppressed the availability of oxygen to the active sites and methane activation over the PdO sites (in the dry feed) was shifted to that over the Pt sites (in the wet feed), as compared with the previous experimental observations of the prevailing chemical state of Pd in the wet feed.

The interaction between bimetals tends to improve stability and water- or carbon dioxide-resistance of the catalyst. Xie *et al.* [32] prepared 3DOM Mn_2O_3-supported $AuPd_y$ alloy (xAuPd$_y$/3DOMMn_2O_3; AuPd loading (x) = 1.0–3.8 wt%; Pd/Au molar ratio (y) = 1.85 and 1.92) catalysts using the PMMA-templating and PVA-protected reduction methods, and their catalytic activities were evaluated for toluene oxidation. It was

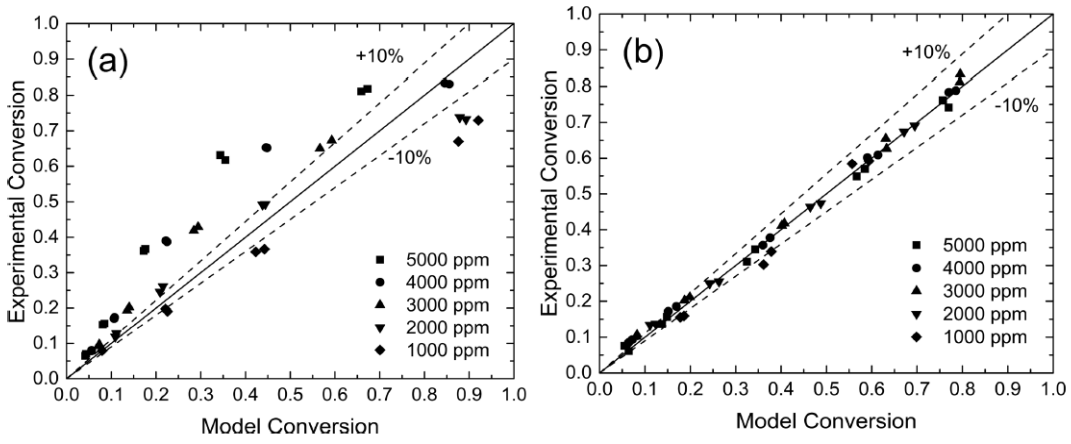

Figure 11: Comparison of the experimental and model conversions using Model 2 for (**a**) dry feed and (**b**) with 5 mol% water added to the feed [31].

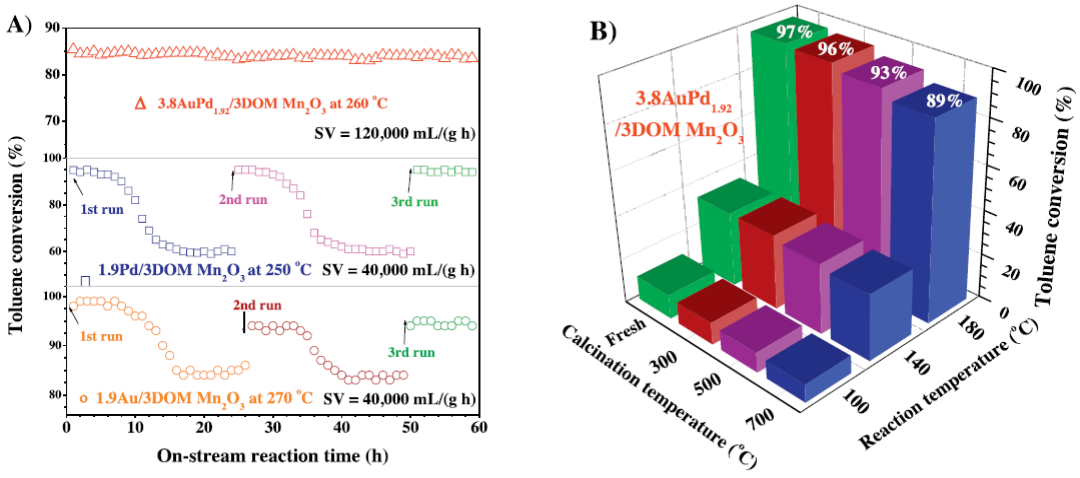

Figure 12: (**A**) Toluene conversion over 1.9Au/3DOM Mn_2O_3 at 270 °C, 1.9Pd/3DOM Mn_2O_3 at 250 °C, and 3.8AuPd$_{1.92}$/3DOM Mn_2O_3 at 260 °C within 60 h of on-stream toluene oxidation at different SVs, and (**B**) toluene conversion versus temperature over the fresh 3.8AuPd$_{1.92}$/3DOM Mn_2O_3sample and the 3.8AuPd$_{1.92}$/3DOM Mn_2O_3sample calcined in N_2 at 300, 500, and 700 °C for 3 h, respectively [32].

found that the AuPd$_y$ alloy NPs with a particle size of 2–4 nm were uniformly dispersed on the 3DOM Mn_2O_3 surface, and the 3.8AuPd$_{1.92}$/3DOM Mn_2O_3 catalyst performed the best: $T_{90\%}$ = 162 °C at 40,000 mL/(g h). Furthermore, 3.8AuPd$_{1.92}$/3DOM Mn_2O_3 was highly active even after calcination at 700 °C (Figure **12**). The introduction of water vapor to the feedstock induced a positive effect on toluene oxidation over 3.8AuPd$_{1.92}$/3DOM Mn_2O_3, but a negative effect over 1.9Au/3DOM-Mn_2O_3 or 1.9Pd/3DOM Mn_2O_3. The authors concluded that the excellent catalytic activity, thermal stability, and water resistance of 3.8AuPd$_{1.92}$/3DOM Mn_2O_3 were associated with its good activation adsorption of oxygen on AuPd$_{1.92}$ NPs and strong interaction between noble metal NPs and 3DOM Mn_2O_3.

The same group also prepared the 3DOM Co_3O_4 and its supported gold–palladium alloy (*x*AuPd/3DOM Co_3O_4; AuPd loading (*x*) = 0.50–1.99 wt%, and Au/Pd mass ratio = 1 : 1) nanocatalysts via the PMMA-templating and PVA-protected reduction routes [33], and found that the 3DOM Co_3O_4-supported Au–Pd catalysts outperformed the supported single Au or Pd catalyst, with the 1.99AuPd/3DOM Co_3O_4 catalyst showing the best activity: the $T_{50\%}$ and $T_{90\%}$ were 164 and 168 °C at a SV of 40,000 mL/(g h), respectively. The 3DOM Co_3O_4-supported Au–Pd nanocatalysts also exhibited better stability and moisture-tolerant ability than the supported Au or Pd catalyst in toluene oxidation (Figure **13**). The apparent activation energies (33–41 kJ/mol) over the *x*AuPd/3DOM Co_3O_4 catalysts

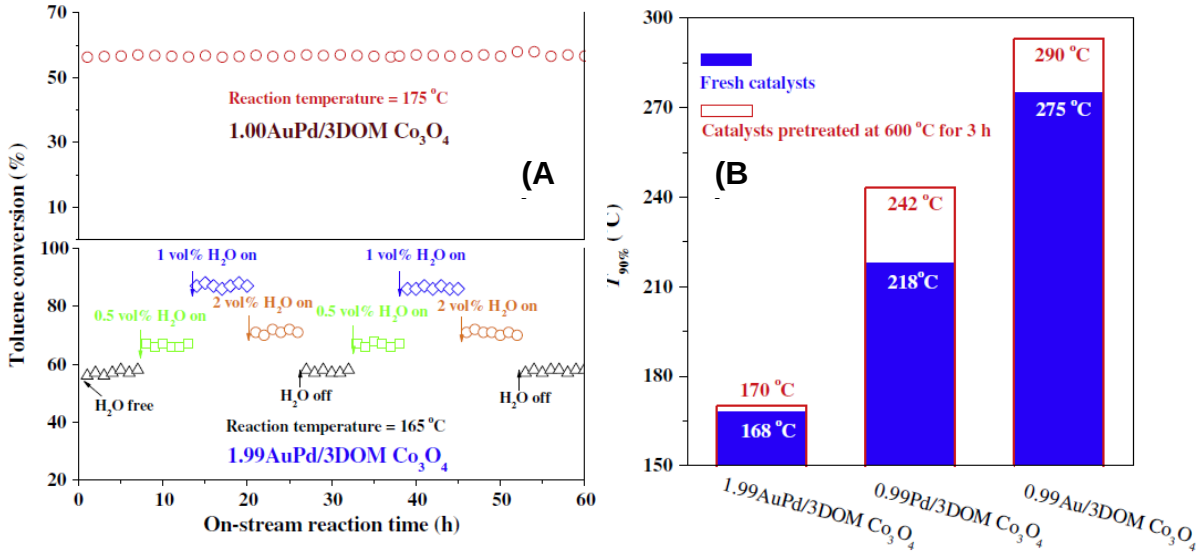

Figure 13: (**A**) On-stream toluene oxidation at 175 °C over 1.00AuPd/3DOM Co_3O_4 and effect of water vapor addition on catalytic activity at 165 °C over 1.99AuPd/3DOM Co_3O_4 at SV = 40,000 mL/(g h), and (**B**) $T_{90\%}$ values for toluene oxidation over the catalysts before and after pretreatment in nitrogen at 600 °C for 3 h [33].

were much lower than those (52–112 kJ/mol) over the 3DOM Co_3O_4 and supported single Au or Pd catalysts, with the 1.99AuPd/3DOM Co_3O_4 catalyst exhibiting the lowest apparent activation energy (33 kJ/mol).

Bimetal catalysts also exhibit good bromine- and chlorine-tolerant performance. For example, Zhang *et al.* [34] synthesized the 3DOM CeO_2-supported Au–Pd alloys (xAuPd$_y$/3DOM CeO_2, x is the total loading (wt%) of Au and Pd, and y is the Pd/Au molar ratio) using the PMMA-templating and PVA-protected reduction methods, and evaluated their activities for the combustion of trichloroethylene (TCE). It was observed that 2.85AuPd$_{1.87}$/3DOM CeO_2 exhibited the highest catalytic activity ($T_{90\%}$ = 415 °C at a SV of 20,000 mL/(g h)) and the lowest apparent activation energy (33 kJ/mol). Besides, 2.85AuPd$_{1.87}$/3DOM CeO_2 showed excellent catalytic stability as well as good moisture- and chlorine-tolerant performance (Figure **14**). The authors believed that alloying of Au with Pd changed the pathway of TCE oxidation and reduced formation of perchloroethylene (PCE), and the factors of highly dispersed AuPd$_{1.87}$ alloy NPs, high adsorbed oxygen species concentration, good low-temperature reducibility, and strong interaction between AuPd$_{1.87}$ NPs and 3DOM CeO_2 as well as high-quality 3DOM structure and high surface acidity were accountable for the excellent catalytic performance of 2.85AuPd$_{1.87}$/3DOM CeO_2.

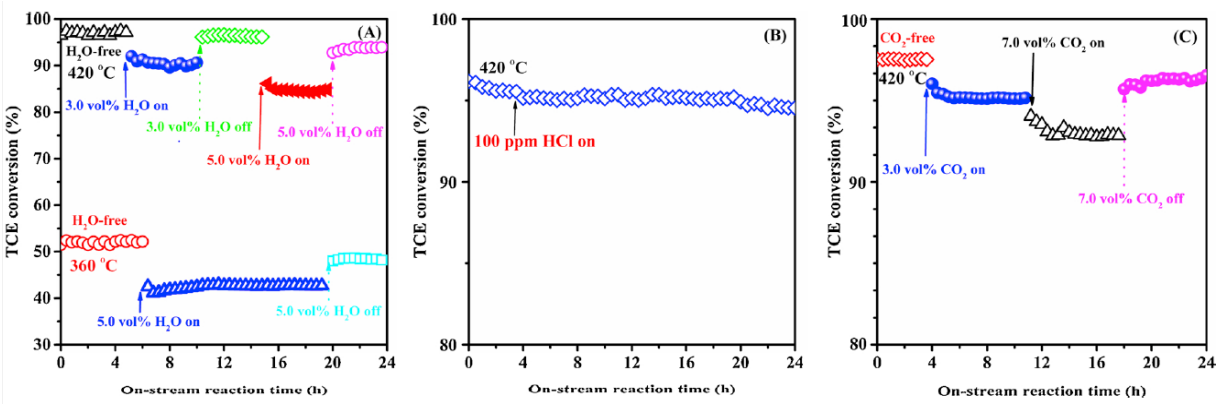

Figure 14: Effects of (**A**) water vapor, (**B**) HCl, and (**C**) carbon dioxide on TCE oxidation over 2.85AuPd$_{1.87}$/3DOM CeO_2 at 420 °C and SV = 20,000 mL/(g h) [34].

3. SUPPORTED NOBLE METAL–TRANSITION METAL CATALYSTS

Although supported noble metal catalysts exhibit good performance for the combustion of VOCs and methane, high noble metal loadings and activity deterioration caused by sintering of noble metals remain the major drawbacks. Therefore, it is of significance to develop more efficient substitutes for industrial applications. A practicable approach of reducing catalyst cost is modification of the noble metals by adding cheap promoters (*e.g.*, transition metal oxides and rare-earth oxides). Doping of the metal oxides (e.g., CeO_2, ZrO_2, NiO, CoO_x, MnO_x, FeO_x, V_2O_5, and WO_3) has been widely accepted as a promising strategy to enhance the activity and stability of catalysts as well as to reduce their cost.

Nanoscale gold exhibits excellent catalytic performance for the oxidation of VOCs and CO, and there have been some catalyst systems containing gold NPs modified by transition metal oxides. For example, Bonelli *et al.* [35] prepared the $Au/FeO_x/CeO_2$ catalysts by impregnating the bimetallic carbonyl cluster salt (*i.e.*, $[NEt_4][AuFe_4(CO)_{16}]$) on the surface of CeO_2, and found that the iron oxide species were homogeneously dispersed on the ceria support surface, and gold NPs grew in particle size with a rise in gold/iron ratio. Addition of the iron oxide species did not substantially increase methanol combustion activity of ceria, but the presence of the mixed gold and FeO_x species could significantly enhance the activity towards the total oxidation of methanol. Qian *et al.* [36] employed the deposition–precipitation method to obtain the $Au/CoO/SiO_2$ catalysts. As shown in Figure **15**, they used the *in situ* infrared spectroscopy to investigate the catalyst preparation process, and found that the gold precursor was deposited preferentially, and interacted with the hydrogen-bonded hydroxyls and the isolated hydroxyls in $Co(OH)_2$ on SiO_2, eventually forming big and small Au NPs on the surface of the support, respectively. The structure and activity of $Au/CoO/SiO_2$ in CO oxidation were dependent on the Au/CoO ratio. Solsona and coworkers [37] fabricated the Co-UVM-7-supported nanosized gold catalysts using the deposition–precipitation methods and investigated the complete oxidation of propane and toluene. The authors claimed that the presence of both gold and cobalt was necessary since the bimetallic Au/Co-UVM-7 catalysts were remarkably more active than the monometallic Au/UVM-7 or Co-UVM-7 catalysts. This phenomenon could be explained on the basis of the enhanced reducibility of some cobalt species in the presence of gold, which facilitated the redox cycle. The good reducibility of cobalt species in the bimetallic

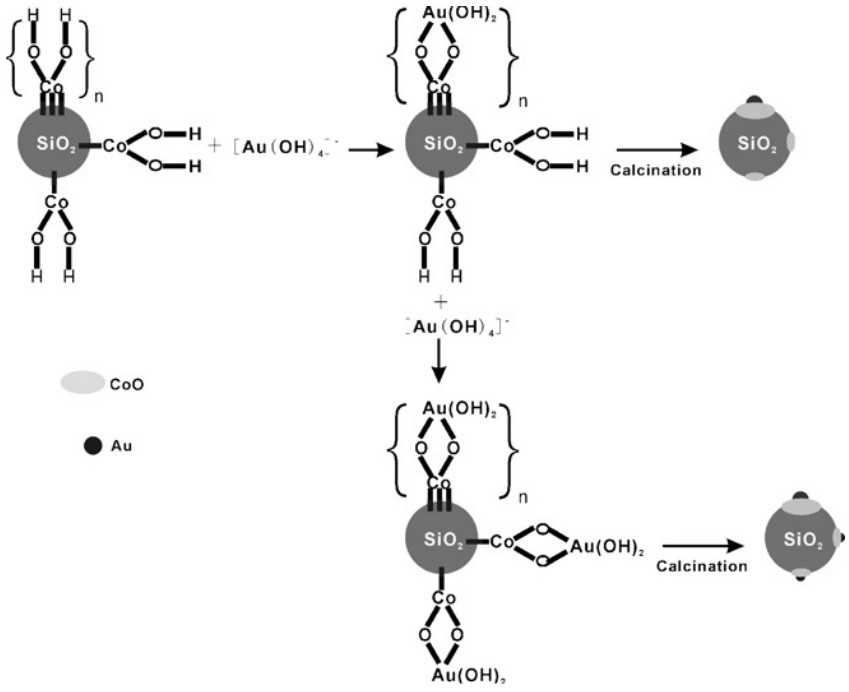

Figure 15: A schematic illustration of the deposition of gold precursor on $Co(OH)_2/SiO_2$ and its influence on the structure of supported Au nanoparticles in $Au/CoO/SiO_2$ catalysts. $Co(OH)_2$ and $\{Co(OH)_2\}_n$ represent isolated $Co(OH)_2$ and $Co(OH)_2$ clusters with hydrogen-bonded hydroxyls on SiO_2, respectively [36].

samples was probably due to formation of the Co_3O_4 domains near the perimeter of the Au–CoO interface, which were absent in the gold-free cobalt-containing catalysts. The authors also observed that these samples showed good stability during the processes of propane and toluene, which could be reasonably explained in terms of the architecture of the siliceous UVM-7 support.

Working on the Au/Al_2O_3 and $Au/MO_x/Al_2O_3$ (M = Cr, Mn, Fe, Co, Ni, Cu, and Zn) catalysts for low-temperature CO oxidation and CH_4 oxidation, Grisel *et al.* [38] pointed out that CO oxidation activity was directly related to the average Au particle size, whereas the identity of MO_x was less important and CH_4 oxidation activity of Au/Al_2O_3 was improved after addition of MnO_x, FeO_x, CoO_x or NiO_x. In recent years, our group have generated the 3D ordered macro-/mesoporous material-supported gold NPs modified by the transition metal oxides. For example, *y*Au/*z*MnO_x/3DOM SiO_2 (*y* = 0–0.95 wt%; *z* = 2.7–15.4 wt%) and *y*Mn_3O_4–*z*Au/3DOM LSCO (*y* = 0.75–2.50 wt%, *z* = *ca.* 2.0 wt%) were fabricated using the PMMA-templating, incipient wetness impregnation, and PVA-protected reduction methods [39,40]. Among these catalysts, 0.93Au/11.2MnO_x/3DOM SiO_2 ($T_{90\%}$ = 255 °C) and 1.67Mn_3O_4–2Au/3DOM LSCO ($T_{90\%}$ = 230 °C) performed the best for toluene oxidation at SV = 20,000 mL/(g h). The good catalytic performance of such materials was ascribed to the higher oxygen adspecies concentration, better low-temperature reducibility, and stronger interaction between Au and MnO_x NPs as well as the unique bimodal porous structure.

The supported palladium catalysts are often used in the combustion of VOCs and methane. As a promoter, transition metal oxides play an important role when they are doped into the Pd NPs. For instance, Fornasiero and coworkers [41] prepared the Si–Al_2O_3-supported Pd@CeO_2 core-shell NPs by a self-assembly method and studied the influence of water vapor on methane combustion over the catalysts. FTIR and CO-chemisorption data indicated that the deactivation caused by water addition of the hierarchical catalyst was due to formation of the stable OH groups on the surface of the ceria NPs. These hydroxyl groups could significantly inhibit the oxygen spillover from CeO_2 to Pd NPs, preventing the efficient re-oxidation, as confirmed by operando X-ray absorption near edge spectroscopic (XANES) results (Figure **16**). Catalytic properties of the Pd@ZrO_2 core-shell catalysts supported on Si-modified alumina as well as the analogous Pd@CeO_2 catalysts were also studied for methane oxidation [42]. It was found that in the absence of water (dry conditions), both Pd@ZrO_2 and Pd@CeO_2 were highly active and showed nearly identical reaction rates and thermal stability. Unlike the catalysts based on Pd@CeO_2, however, the Pd@ZrO_2 catalysts were rather stable in the presence of high water vapor concentrations. Using the Coulometric titration and pulse-reactor, the authors demonstrated

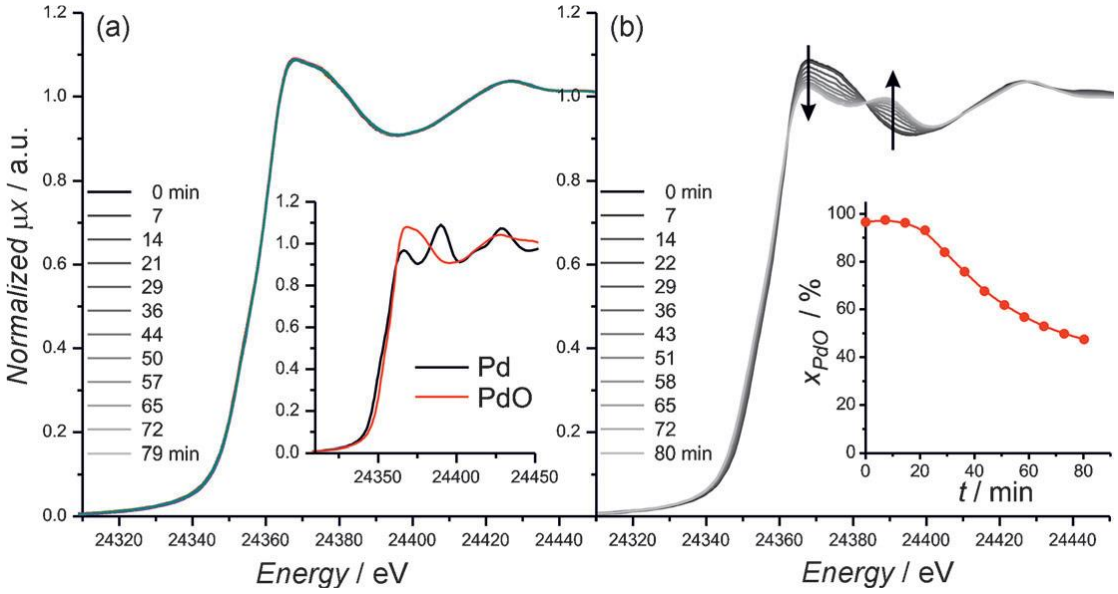

Figure 16: Normalized XANES spectra obtained during operando methane combustion under (**a**) dry and (**b**) wet reaction conditions at 600 °C. Conditions: 0.5 vol% CH_4, 2.0 vol% O_2, 15.0 vol% H_2O (if present), N_2 balance. The insets report XANES of reference Pd and PdO and PdO percentage during wet reaction conditions at 600 °C, respectively [41].

that ZrO_2 in contact with Pd could be reduced, and the Pd–PdO equilibrium at 600 °C was shifted to much lower P_{O2} in the Pd@ZrO_2 catalyst, as compared with the conventional Pd/ZrO_2 or Pd/Al_2O_3 catalyst. Such an observation could explain the superior catalytic performance of Pd@ZrO_2 that was due to the fact that PdO is more active for methane oxidation. Satsuma *et al.* [43] probed the effect of preparation method ((i) co-impregnation of an aqueous solution of palladium nitrate and cobalt nitrate mixture; and (ii) sequential impregnation of an aqueous solution of cobalt nitrate to Pd/alumina) on methane combustion over the Co-promoted Pd/alumina catalysts, and found that the co-impregnated catalysts showed higher activities than the un-promoted Pd/alumina catalyst, while the sequentially impregnated catalysts showed lower activities. The result of methane-temperature programmed reduction revealed that the better dispersion of Co on Pd resulted in better reducibility of the Pd species, which was attributed to the higher methane oxidation activity of the co-impregnated catalysts. Qi *et al.* [44] fabricated the Pd- and CeO_2-promoted Co/Al_2O_3 catalysts via a wet co-impregnation route and investigated the influence of Pd, Ce, and Co/Ce molar ratios on the catalytic performance of Co/Al_2O_3 for benzene oxidation. The results indicated that the high activity was mainly due to the better-dispersed Co_3O_4 on Al_2O_3, smaller Co_3O_4 crystallites, and larger CeO_2 crystallites, which could strengthen the interaction between PdO or CeO_2 and Co_3O_4. In addition, we also studied the influence of Pd NPs modified by the transition metal oxides on the combustion of the typical VOC or methane. For instance, the 3DOM CeO_2 and its supported Pd@Co (Co_xPd/3DOM CeO_2, *x* (Co/Pd molar ratio) = 2.4–13.6) nanocatalysts were prepared using the PMMA-templating and modified PVA-protected reduction methods [45], respectively. The Pd@Co particles displayed a core-shell (core: Pd; shell: Co) structure with an average size of 3.5–4.5 nm and were uniformly dispersed on the surface of 3DOM CeO_2. As shown in Figure **17**, $Co_{3.5}$Pd/3DOM CeO_2 showed the highest activity ($T_{90\%}$ = 480 °C at a SV of 40,000 mL/(g h) and excellent stability in the range 400–800 °C. We concluded that the excellent catalytic performance of $Co_{3.5}$Pd/3DOM CeO_2 was associated with its good ability to adsorb oxygen and methane as well as the unique core-shell structure of CoPd NPs. In another work, we adopted a novel strategy (i.e., the oxidative transformation of intermetallic Pd_5Ga_3 nanocrystals supported on Al_2O_3) to generate the GaO_x-doped Pd/Al_2O_3 catalysts [46]. There was a synergistic effect between palladium and gallium oxide via formation of a bi-functional active Pd–O–Ga phase, resulting in a highly active and exceptionally stable catalyst that could markedly suppress the sintering of noble metals under harsh conditions (hydrothermal treatment at 750 °C). Moreover, the presence of a large amount of surface oxygen vacancies and the surface Pd–O–Ga phase could promote methane combustion over the catalysts.

Eguchi and coworkers [47] investigated the palladium catalysts (Pd/Al_2O_3–MO_x; M = Co, Cr, Cu, Fe, Mn, and Ni) supported on the mixed oxides for the

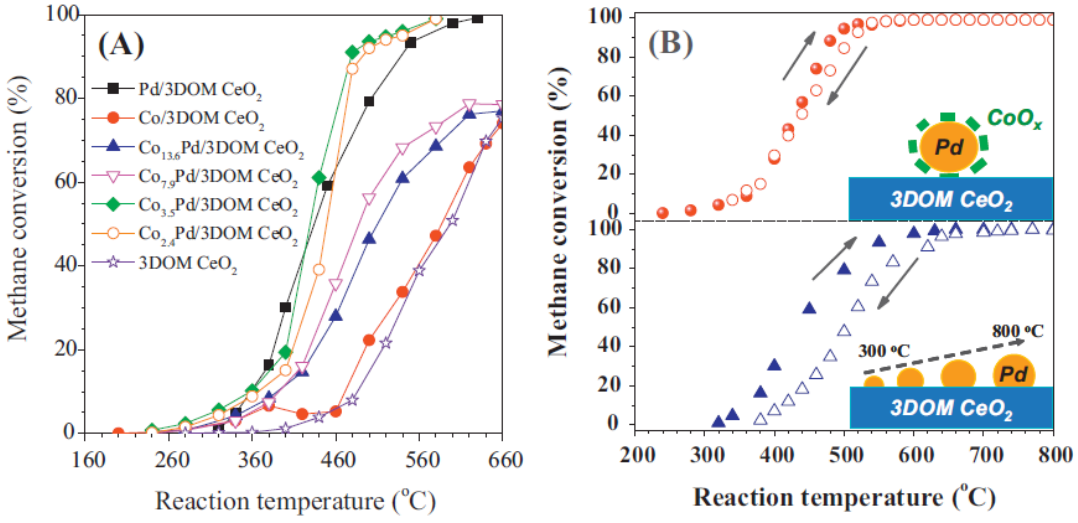

Figure 17: (**A**) Methane conversion as a function of reaction temperature over the as-prepared samples at SV = 40,000 mL/(g h) and (**B**) methane conversion versus temperature when the activity was measured with the rise in temperature (solid) or the drop in temperature (empty) over the $Co_{3.5}$Pd/3DOM CeO_2 and Pd/3DOM CeO_2 samples [45].

low-temperature combustion of methane, and found that Pd/Al_2O_3–36NiO exhibited an excellent activity due to the small particle size of palladium. The results of temperature-programmed desorption of oxygen revealed that catalytic activity in the low-temperature region depended upon the adsorption state of oxygen on palladium and it enhanced when amount of the adsorbed oxygen species increased. The *in situ* XRD analysis results indicated that the PdO phase in Pd/Al_2O_3–36NiO was thermally stable. Zou *et al.* [48] proposed a facile strategy to stabilize the catalytic performance of Pd/Al_2O_3 by introducing a spinel-type $NiAl_2O_4$ interface as a promoter. A series of 0.4 wt% Pd/*x*NiO/γ-Al_2O_3 catalysts with NiO loadings of 0–9.0 wt% were fabricated. The formation of a $NiAl_2O_4$ interface promoted the distribution and crystallization of PdO, suppressed aggregation of the PdO particles and accumulation of the surface OH^- species during the reaction process, hence giving rise to the excellent catalytic performance. After investigating the role of vanadium oxide and palladium in the oxidation of benzene over the Pd/V_2O_5/Al_2O_3 catalysts, Ferreira *et al.* [49] pointed out that Pd/V_2O_5/Al_2O_3 was more active than V_2O_5/Al_2O_3 and Pd/Al_2O_3. The increase of vanadia content decreased Pd dispersion and increased benzene conversion. A strong effect of Pd particle size on benzene oxidation was observed. Although the catalysts containing high amounts of the V^{4+} species were more active, the Pd particle size effect was responsible for the higher activity. Xie *et al.* [50] developed a novel approach by introducing a certain amount of CoO to the supported Au–Pd alloy NPs, thus generating the high-performance Au–Pd–*x*CoO/3DOM Co_3O_4 catalysts. Doping of CoO induced formation of the PdO–CoO active sites, which was beneficial for the improvements in adsorption and activation of CH_4 and hence in catalytic performance. This nanocatalyst exhibited better thermal stability and water-tolerant ability, as compared with the 3DOM Co_3O_4-supported Au–Pd or Pd–CoO nanocatalyst.

The addition of the transition metal oxides in the supported platinum catalysts may effectively improve catalytic activity and stability by increasing the interfacial surface between Pt and transition metal oxide. For example, Sedjame *et al.* [51] generated Pt catalysts supported on CeO_2–Al_2O_3 (in which ceria contents were 0–51 wt%) by the sol-gel method, and found that doping of ceria resulted in the improvement in catalytic activity for *n*-butanol or acetic acid oxidation even if it also gave rise to formation of numerous intermediate products, which were mainly attributed to the actives sites of ceria. Jeong *et al.* [52] prepared the Pt/CeO_2–ZrO_2–NiO/γ-Al_2O_3 catalysts using the coprecipitation and impregnation methods. The authors claimed that the complete oxidation of toluene was realized at the temperature as low as 100 °C over the 10 wt% Pt/16 wt% $Ce_{0.64}Zr_{0.16}Ni_{0.2}O_{1.9}$/$\gamma$-$Al_2O_3$ catalyst. Introduction of a small amount of NiO to the cubic fluorite-type CeO_2–ZrO_2 structure was considerably effective to enhance the oxygen release and storage ability due to formation of oxygen vacancies and Ni^{2+}/Ni^{3+} redox couples. Jiang *et al.* [53] prepared an atomically dispersed Pt_1–Co_3O_4 catalyst via an ethylene glycol reduction route, and observed that the Pt_1–Co_3O_4 catalyst exhibited an exceptionally high efficiency in the total oxidation of methanol. As shown in Figure (**18**), the experimental and theoretical investigation results indicated that this catalyst consisted of the Pt sites with a large proportion of the occupied high electronic states. These sites possessed a strong affinity to the inactive Co^{2+} sites and were anchored on the (111) crystal plane, which increased the metal–support interaction of the Pt_1–Co_3O_4 material and accelerated the rate of oxygen vacancy regeneration. The density functional theory calculation results confirmed that the electron transfer of oxygen vacancies reduced methanol adsorption energy and activation barrier, thus significantly enhancing dissociation of the C–H bonds in methanol molecules. Wittayakun and coworkers [54] investigated adsorption of ethanol on the bimetallic catalysts containing 0.5 wt% Pt and 15 wt% Co, Cu or Mn oxide supported on RH-MCM-41 by the temperature-programmed desorption (ethanol-TPD) and thermogravimetric analysis (ethanol-TGA), and found that the transition metal oxide could serve as a potential oxygen supplier in ethanol oxidation. In the monometallic catalyst containing oxides of Co, Cu or Mn oxide on RH-MCM-41, cobalt oxide was a better oxygen supplier, as compared with the other two metal oxides. The bimetallic 0.5Pt–15Co/RH-MCM-41 catalyst with cobalt being in the form of Co_3O_4 showed the highest ethanol adsorption and CO_2 desorption, and the bimetallic catalysts exhibited lower ethanol conversions than the monometallic Pt catalyst, but seemed to be more stable than the latter.

Previously, our group prepared the 3DOM Al_2O_3-supported cobalt oxide and platinum (*x*Pt/*y*Co_3O_4/3DOM Al_2O_3, Pt content (*x*) = 0–1.4 wt%, and Co_3O_4 content (*y*) = 0–9.2 wt%) nanocatalysts using the PMMA-templating, incipient wetness impregnation and PVA-protected reduction approaches [55]. Among

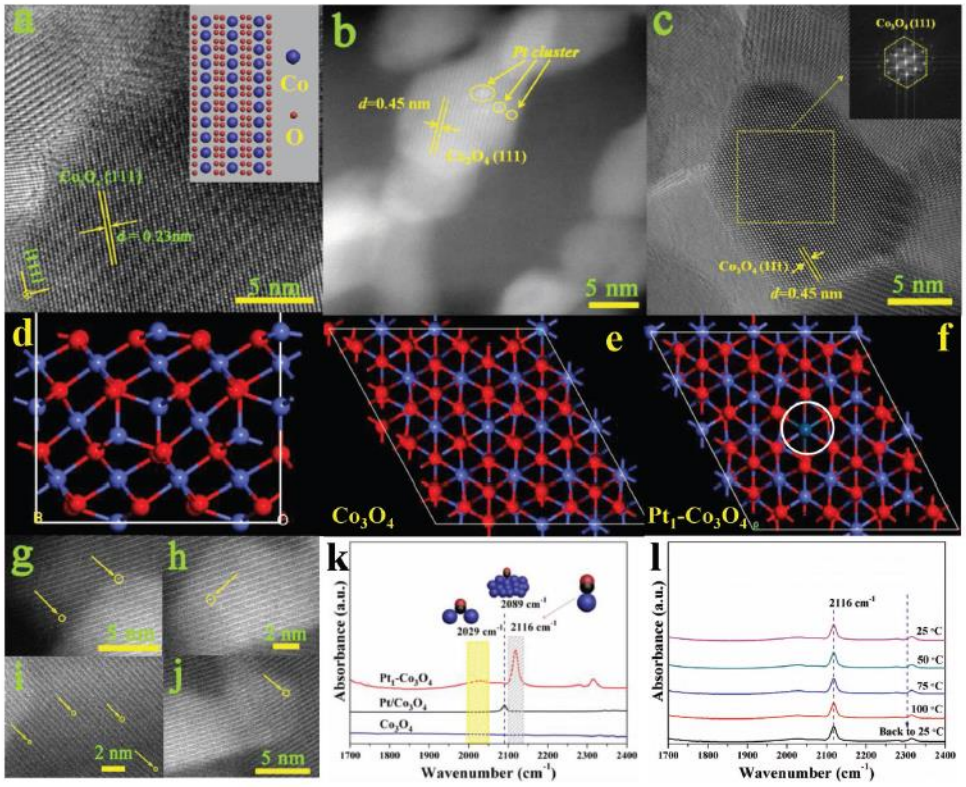

Figure 18: (**a**–**c**) HRTEM images of Co_3O_4, Pt/Co_3O_4, and Pt_1–Co_3O_4 samples; (**d**–**f**) stable structure models optimized by theoretical calculations; (**g**–**j**) aberration-corrected HAADF–STEM images of Pt_1–Co_3O_4 material; (**k**) *in situ* FTIR spectra of CO adsorption over prepared samples; (**l**) temperature-dependent CO adsorption over Pt_1–Co_3O_4 catalyst [53].

these catalysts, 1.3Pt/8.9Co_3O_4/3DOM Al_2O_3 performed the best in toluene oxidation, with a $T_{90\%}$ of 160 °C at a SV of 20,000 mL/(g h). We believed that the excellent catalytic performance was owing to the well-dispersed Pt NPs, high adsorbed oxygen species concentration, good low-temperature reducibility, and strong interaction between Pt or Co_3O_4 NPs and 3DOM Al_2O_3 as well as the unique bimodal porous structure of the support. Working on the $Pt_{0.3}Mn_x/SiO_2$ nano cubic (nc) micro-/mesoporous composite catalysts with various Mn contents (derived from an ethylene glycol reduction route) for the oxidation of methyl ethyl ketone (MEK), He and coworkers [56] realized that MEK could be efficiently oxidized over the $Pt_{0.3}Mn_x/SiO_2$-nc catalysts, with the reaction rate and turnover frequency being higher than 12.7 mmol/(g_{Pt} s) and 4.7 s^{-1} at 100 °C, respectively. The remarkable performance of the material was attributed to a synergistic effect between Pt NPs and Mn_2O_3. Results of NH_3-TPD and NH_3-FTIR characterization revealed that the exposed Mn_2O_3 (222) facets enhanced the quantity of Brønsted acid sites in the catalyst, which were responsible for promoting desorption of the adsorbed O_2 and CO_2 species. Moreover, $^{18}O_2$ isotopic labeling results demonstrated that the presence of a Pt–O–Mn moiety weakened the Mn–O bonding interaction, ultimately promoting the mobility of lattice oxygen in Mn_2O_3. As shown in Figure **19**, the Mn^{4+}/Mn^{3+} redox cycle in Mn_2O_3 allowed for donation of the electrons to the Pt NPs, enhancing the Pt^0/Pt^{2+} proportion and hence increasing activity and stability of the catalyst. Hou *et al.* [57] prepared the Pt/$Ce_{0.65}Zr_{0.35}O_2$ and Pt–WO_3/$Ce_{0.65}Zr_{0.35}O_2$ catalysts using the incipient-wetness impregnation strategy, and observed that Pt–WO_3/$Ce_{0.65}Zr_{0.35}O_2$ performed better than Pt/$Ce_{0.65}Zr_{0.35}O_2$ for the oxidation of toluene. On the basis of the characterization results, the authors concluded that the good low-temperature reducibility, higher surface adsorbed oxygen concentration, and medium-strong acidity was responsible for the excellent catalytic activity of Pt–WO_3/$Ce_{0.65}Zr_{0.35}O_2$. More recently, our group have prepared the 3DOM $CoFe_2O_4$, *z*MnO_x/3DOM $CoFe_2O_4$ (*z* = 4.99–12.30 wt%), and *y*Pd–Pt/6.70 wt% MnO_x/3DOM $CoFe_2O_4$ (*y* = 0.44–1.81 wt%; Pd/Pt molar ratio = 2.1–2.2) using the PMMA microspheres-templating, incipient wetness impregnation, and bubble-assisted PVA-protected reduction strategies [12]. It was observed that loading of MnO_x on $CoFe_2O_4$ gave rise to a slight increase in activity, however, the dispersion of Pd–Pt NPs on 6.70MnO_x/3DOM

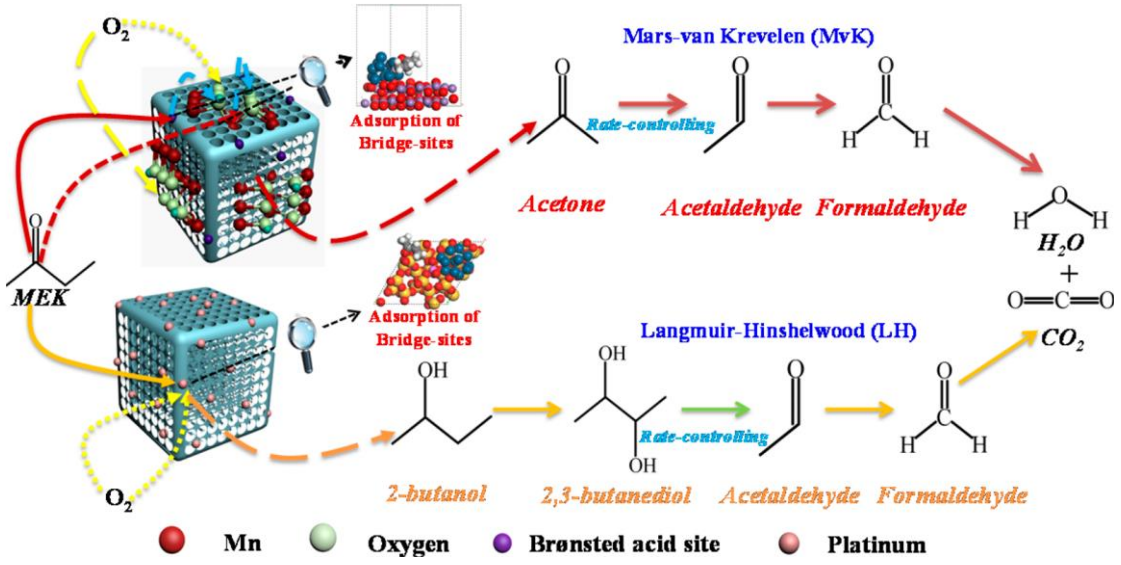

Figure 19: Reaction mechanism for catalytic MEK oxidation over the $Pt_{0.3}/SiO_2$-nc and $Pt_{0.3}Mn_5/SiO_2$-nc catalysts [56].

$CoFe_2O_4$ significantly enhanced the catalytic performance, with the $1.81Pd_{2.1}Pt/6.70MnO_x$/3DOM $CoFe_2O_4$ sample performing the best ($T_{90\%}$ = 372 °C at a SV of 20,000 mL/(g h)). We thought that the excellent catalytic activity of $1.81Pd_{2.1}Pt/6.70MnO_x$/3DOM $CoFe_2O_4$ was related to its well-dispersed Pd–Pt alloy NPs, high adsorbed oxygen species concentration, good low-temperature reducibility, and strong interaction between MnO_x or Pd–Pt NPs and 3DOM $CoFe_2O_4$.

4. SUPPORTED NON-PRECIOUS BIMETAL CATALYSTS

It is well known that transition metals, especially transition bimetals, are effective components in constituting high-performance catalysts for the removal of VOCs and CVOCs. Zeolitic materials possess rich porous structures, high surface areas, and appropriate acidity and basicity, which are beneficial for the adsorption of VOCs and CVOCs and hence improvement in catalytic performance. For example, Zhou and coworkers [58] fabricated the CeO_2- and/or CuO-modified zeolitic USY catalysts by the impregnation method, and examined their catalytic behaviors for the oxidation of CVOCs as well as their stability after long exposure to 1,2-chloroethane (DCE). The CuO–CeO_2/USY catalyst with the respective CuO and CeO_2 loadings of 16.9 and 12.5 wt% showed the best activity for DCE removal ($T_{90\%}$ = 288 °C at a DCE concentration of 1000 ppm and a SV of 15,000 mL/(g h)). The better performance of the CeO_2–CuO-modified USY catalyst was ascribed to its high dispersion of the active phases (CeO_2 or CuO), improved mobility of the active oxygen species, and increment of the Lewis acidity. The addition of CeO_2 and CuO improved the durability of the catalyst after the long-term exposure to DCE, which was due to the slight coke deposition and preserved high density of the acid sites. Huang *et al.* [59] prepared the chromium- and cerium-modified USY (Cr_2O_3–CeO_2/USY) catalysts by the impregnation method, and investigated catalytic oxidation of dichloromethane (DCM) or TCE. The authors pointed out that the interaction between the Cr_2O_3 and CeO_2 species optimized the concentration ratio of strong acid sites to weak acid sites, and improved the mobility of oxygen species on the Cr_2O_3-CeO_2/USY catalysts, which were beneficial for dehydrochlorination and deep oxidation of CVOCs, respectively. The 17.5 wt% Cr_2O_3–12.5 wt% CeO_2/USY catalyst showed better performance along with higher selectivity to HCl and CO_2 for CVOCs removal. Under the conditions of DCM or TCE concentration = 1000 ppm and SV = 15,000 mL/(g h), catalytic activity for DCM destruction decreased in the order of 17.5 wt% Cr_2O_3–12.5 wt% CeO_2/USY ($T_{90\%}$ = 281 °C) > 12.5 wt% CeO_2–USY ($T_{90\%}$ = 340 °C) > USY ($T_{90\%}$ = 370 °C), and that for TCE removal followed a sequence of 17.5 wt% Cr_2O_3–12.5 wt% CeO_2/USY ($T_{90\%}$ = 296 °C) > 12.5 wt% CeO_2–USY ($T_{90\%}$ = 422 °C) > USY ($T_{90\%}$ = 515 °C), which were due to the higher percentage of strong acidity, more accessible oxygen species, and stronger synergistic action between Cr_2O_3–CeO_2 and USY. In addition, the stronger interaction between Cr_2O_3 and CeO_2 as well as that between Cr_2O_3–CeO_2 and USY in 17.5 wt% Cr_2O_3–12.5 wt% CeO_2/USY gave rise to less coke deposition, slight HCl attack on the catalyst, and

improved resistance to chlorination of the active components. Hence, 17.5 wt% Cr_2O_3–12.5 wt% CeO_2/USY possessed better durability and structure stability after the long-term exposure to DCE.

Working on the silicon tetrachloride-modified H-ZSM-5 (Si/Al = 240)-supported chromium and/or copper ($Cr_{1.5}/SiCl_4$-Z, $Cu_{1.5}/SiCl_4$-Z, and $Cr_{1.0}Cu_{0.5}/SiCl_4$-Z) catalysts for the combustion of DCM, trichloromethane (TCM), and TCE, Abdullah *et al.* [60] found that treatment of the catalyst with silicon tetrachloride could improve the chemical resistance of H-ZSM-5 against hydrogen chloride, and the 1.5 wt% $Cr_{1.0}Cu_{0.5}/SiCl_4$-Z catalyst exhibited good performance for the destruction of DCM, TCM, and TCE with $T_{90\%}$ = 328, 300, and 375 °C, respectively. TCM was more reactive than DCM, but oxidation of the former produced a more amount of by-products due to its high chlorine content. The stabilization of TCE was attributed to its resonance effect. Water vapor increased carbon dioxide yield since it could play roles of a hydrolysis agent forming reactive carbocations and a hydrogen-supplying agent suppressing the chlorine-transfer reactions. Yang *et al.* [61] generated the various zeolites-supported (Ce, Cr)$_x$O$_2$ catalysts with a Ce/Cr molar ratio of 4 and a (Ce,Cr)$_x$O$_2$ loading of 40 wt% via a precipitation route, and evaluated their catalytic activities for the deep oxidation of DCE. In terms of $T_{90\%}$ at a DCE concentration of 1000 ppm and a SV of 9,000 mL/(g h), catalytic activity decreased in the order of (Ce,Cr)$_x$O$_2$/HZSM-5 (230 °C) > (Ce,Cr)$_x$O$_2$/H-BETA (243 °C) > (Ce,Cr)$_x$O$_2$/USY (247 °C) > (Ce,Cr)$_x$O$_2$/H-MOR (253 °C) (Figure **20**), which was due to the existence of a synergistic effect between (Ce,Cr)$_x$O$_2$ and zeolite. The strong acid sites of the zeolite firstly promoted DCE adsorption and dehydrochlorination, while the strong oxidative sites of (Ce,Cr)$_x$O$_2$ were in favor of deep oxidation of the reactants, intermediates, and by-products as well as reduction of the coke and Cl accumulation on the catalyst surface. Especially, (Ce,Cr)$_x$O$_2$/HZSM-5 showed the best catalytic activity, which was related to its special intersectional pore structure. Moreover, although the presence of benzene or water decreased the catalytic activity in the initial stage due to their competitive adsorption on the active sites, the (Ce,Cr)$_x$O$_2$/HZSM-5 catalyst possessed good durability in the prolonged reaction time.

Working on the Na-montmorillonite (Na-mmt) and different pillared interlayered clays (Al-PILC, Zr-PILC, Ti-PILC and Al_2O_3/Ti-PILC)-supported CrCe catalysts for the deep oxidation of nitrogen-containing VOCs (NVOCs), Huang *et al.* [62] pointed out that porous structure and acidity played important roles in the addressed reaction. The mesoporous structure and proper acid sites improved catalytic activity of the supported CrCe catalysts. At the total Cr and Ce content of 8 wt% with a Cr/Ce molar ratio of 6 : 1, the catalytic activity decreased in the sequence of CrCe/Al_2O_3/Ti-PILC ($T_{50\%}$ = 170 °C) > CrCe/Ti-PILC ($T_{50\%}$ = 180 °C) > CrCe/Zr-PILC ($T_{50\%}$ = 210 °C) > CrCe/Al-PILC ($T_{50\%}$ = 240 °C) > CrCe/Na-mmt ($T_{50\%}$ = 260 °C). Among all of the catalysts, CrCe/Ti-PILC and CrCe/Al_2O_3/Ti-PILC exhibited much higher catalytic activity than the other catalysts at a SV of 20,000 mL/(g h) and a *n*-butylamine concentration of 1000 ppm. *N*-

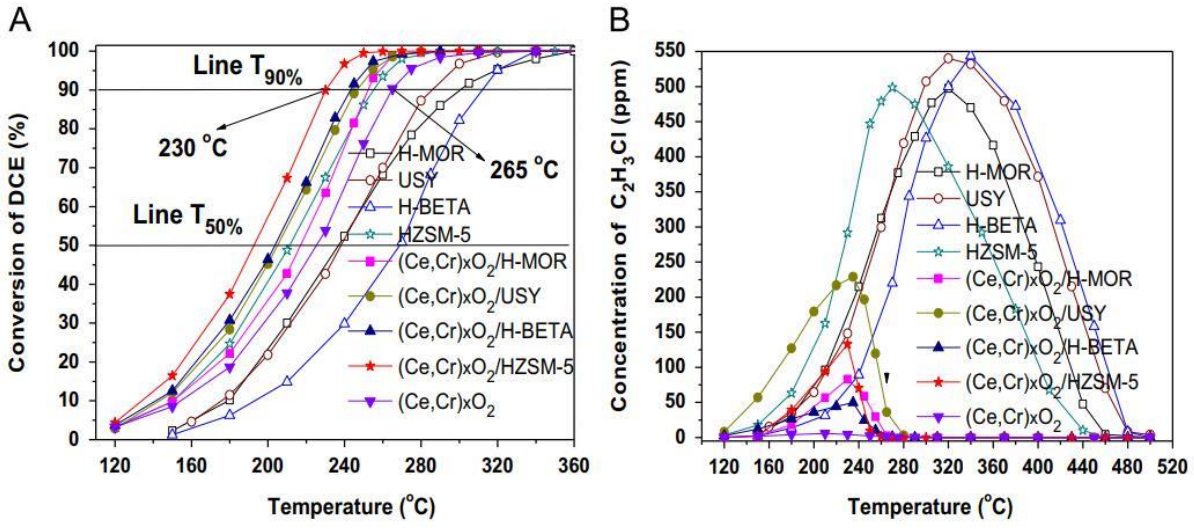

Figure 20: Catalytic performance for deep oxidation of DCE over the catalysts: (**A**) Conversion of DCE and (**B**) concentration of byproduct C_2H_3Cl [61].

butylamine and ethylenediamine with $–NH_2$ groups were easier to be destructed due to their stronger adsorption on the acid sites of the catalysts, but too strong adsorption of ethylenediamine on the acid sites could lead to a lower activity, as compared with the adsorption of *n*-butylamine on the acid sites. Using a one-step hydrothermal, ion exchange, and impregnation methods, Feng *et al.* [63] generated the AlZr-pillared clay (AlZr-PILC) and its supported manganese and cerium oxide catalysts. The as-synthesized AlZr-PILC outperformed the raw Na-montmorillonite clay (Na-mmt) and Al-PILC in the combustion of chlorobenzene (CB), and the high activity of the former was related to the high dispersion of the oxides and the exposure of more active sites. Loading of ceria could promote the redox cycle of the manganese-loaded catalyst system through the strong interaction between MnO_2 or CeO_2 and AlZr-PILC. In particular, 2 wt% MnCe(9 : 1)/AlZr-PILC showed high catalytic activity and CB was completely degraded at approximately 280 ^oC (reaction conditions: CB concentration = 1000 ppm and SV = 20,000 mL/(g h)). Compared with Mn/AlZr-PILC, MnO_2 in the MnCe(9 : 1)/AlZr-PILC catalyst was more readily reduced, which indicated that doping of CeO_2 could significantly improve the CB oxidation performance. By adopting an impregnation strategy, Zuo *et al.* [64] fabricated the Ti-pillared clay (Ti-PILC)-supported CrCe oxides with large surface areas, uniform mesopores, and high thermal stability. It was observed that 10 wt% CrCe(6 : 1)/Ti-PILC enabled the CB to be completely degraded at 250 ^oC under the conditions of 500 ppm CB and SV = 20,000 mL/(g h), which was much higher than those of the other catalysts. Furthermore, the porous structure of the support remained stable after calcination at 550 ^oC, and the active phases were evenly dispersed on the support surface without a significant aggregation, indicating that the material was a promising catalyst for CB removal.

Kan *et al.* [65] prepared the 20 wt% MnCe/cordierite and Mn–Co–Ce/cordierite catalysts with different metal molar ratios (Figure **21**), and studied their catalytic activities for low-concentration CB (500 ppm) oxidation. Among the 20 wt% MnCe/cordierite catalysts at SV = 15,000 mL/(g h), the catalytic activity decreased in the order of Mn_4Ce_1/cordierite ($T_{90\%}$ = 364 ^oC) > Mn_2Ce_1/cordierite ($T_{90\%}$ = 375 ^oC) > Mn_1Ce_1/cordierite ($T_{90\%}$ = 382 ^oC); Among the Mn–Co–Ce/cordierite catalysts at SV = 15,000 mL/(g h), the catalytic activity decreased in the sequence of $Mn_8Co_1Ce_1$/cordierite ($T_{90\%}$ = 325 ^oC) > $Mn_3Co_1Ce_1$/cordierite ($T_{90\%}$ = 337 ^oC) > $Mn_2Co_2Ce_1$/cordierite ($T_{90\%}$ = 350 ^oC). Obviously, Mn_4Ce_1/cordierite and $Mn_8Co_1Ce_1$/cordierite performed the best. In addition, the $Mn_8Co_1Ce_1$/cordierite sample was catalytically stable during the long-term CB oxidation at 350 ^oC. The good performance of the supported $Mn_8Co_1Ce_1$ catalyst was primarily due to the

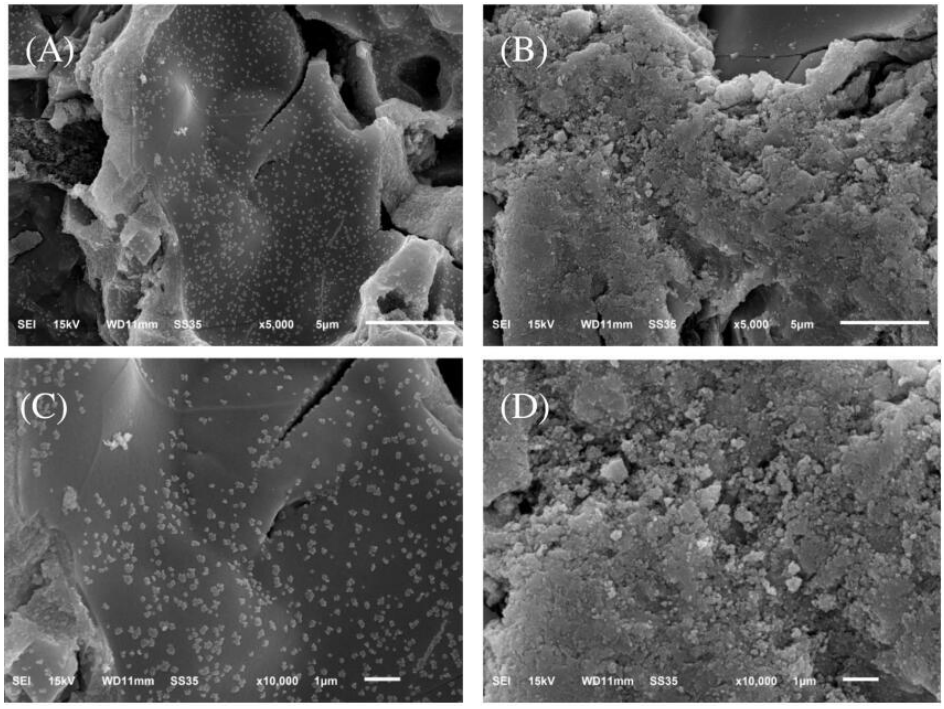

Figure 21: SEM images of (**A**, **C**) $Mn_8Co_1Ce_1$/cordierite and (**B**, **D**) Mn_4Ce_1/cordierite [64].

synergistic effect of ceria, manganese, and cobalt, which could promote formation of more amounts of the lattice defects and oxygen vacancies as well as the smaller crystallite size.

Yang *et al.* [66] prepared the CeO_2 and/or Cr_2O_3 catalysts supported on HZSM-5 (SiO_2/Al_2O_3 molar ratio = 22) by the impregnation method, and investigated their catalytic properties for the removal of TCE. It was found that the sequence in catalytic activity for TCE destruction was as follows: 9 wt% Cr–12 wt % CeO_2/HZSM-5 ($T_{90\%}$ = 269 °C) > 9 wt% Cr/HZSM-5 ($T_{90\%}$ = 314 °C) > 21 wt% Cr/HZSM-5 ($T_{90\%}$ = 333 °C) > 21 wt% CeO_2/HZSM-5 ($T_{90\%}$ = 339 °C) > 12 wt% CeO_2/HZSM-5 ($T_{90\%}$ = 347 °C) > HZSM-5 ($T_{90\%}$ = 482 °C) at a TCE concentration of 1000 ppm and a SV of 15,000 mL/(g h), with 9 wt% Cr–12 wt% CeO_2/HZSM-5 exhibiting the best catalytic activity and durability. The characterization results revealed that the interaction between CeO_2 and Cr_2O_3 increased the amount of Cr^{6+} species with a strong oxidation ability and promoted the mobility of the active oxygen species in the metal oxide-modified HZSM-5 catalyst, which were beneficial for the deep oxidation of the intermediates produced in the destruction process of the CVOC and the improvement in resistance to coke deposition. The synergy between CeO_2 or Cr_2O_3 and HZSM-5 could promote the dehydrochlorination of TCE as well as the formation of suitable strong and weak acidity ratio, which was also in favor of improving catalytic degradation of the CVOC. Sun *et al.* [67] used a wet impregnation route to generate the $Mn_xCe_{1-x}O_2$/H-ZSM5 catalysts, and studied their catalytic properties in CB oxidation under the dry or humid conditions. The 20 wt% $Mn_{0.8}Ce_{0.2}O_2$/H-ZSM5 catalyst possessed the highest activity ($T_{90\%}$ = 230 °C at a CB concentration of 1000 ppm and a SV of 10,000 mL/(g h)). *In situ* DRIFTS results revealed that under the dry condition, the H-ZSM5 could promote the dissociation of CB from its aromatic ring to Cl•, and the aromatic ring was transformed into the cyclohexanone or benzoquinone species, hence facilitating the CB ring-opening process. Under the humid condition, the presence of H_2O could not only protect the active sites of $Mn_{0.8}Ce_{0.2}O_2$ from the poisoning by the accumulated chlorine, but also act as the H• and OH• radical sources to deeply oxidize CB, thus promoting the production of HCl and CO_2 over the $Mn_xCe_{1-x}O_2$/H-ZSM5 catalyst.

Chen *et al.* [68] prepared the paper-like sintered stainless-steel fiber (PSSF)-supported Cu–Mn binary oxide-modified ZSM-5 membrane catalysts (Figure **22**) by the lay-up papermaking/sintering, incipient wetness

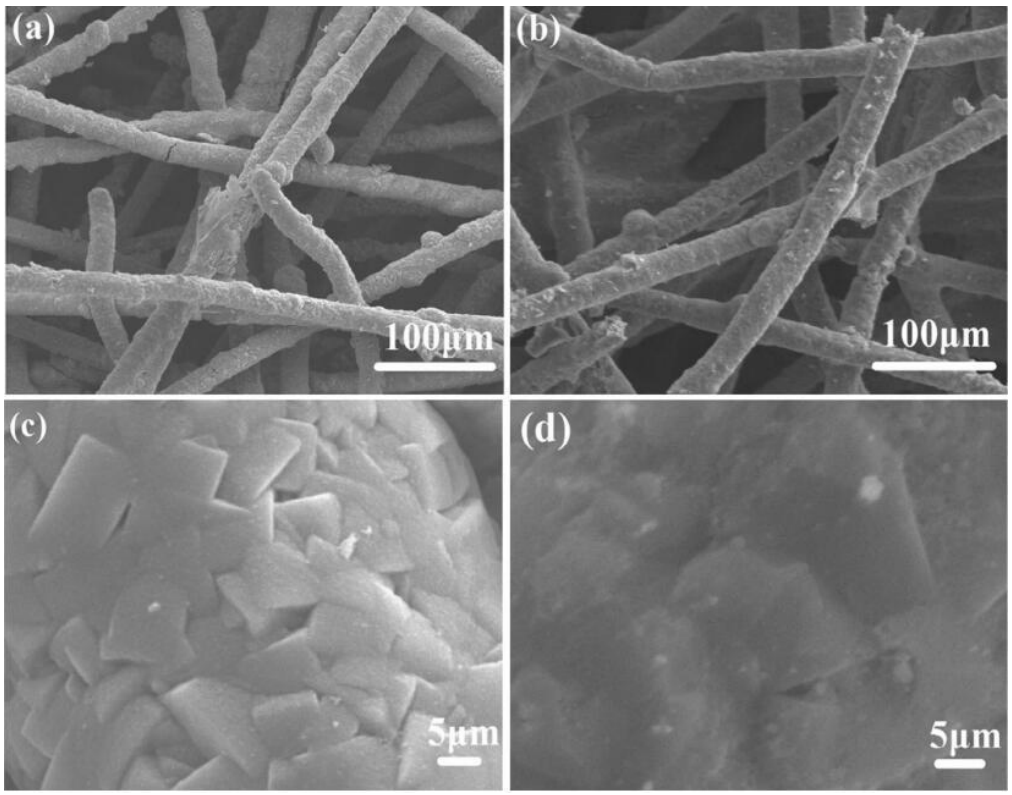

Figure 22: SEM images of (a) ZSM-5 membrane/PSSF, (b, d) Cu–Mn(1 : 6)/ZSM-5/PSSF, and (c) ZSM-5 membrane [68].

impregnation, and secondary growth methods, and found that the 46 wt% Cu–Mn(1 : 6)/ZSM-5/PSSF catalyst exhibited the best activity for the oxidation of isopropanol ($T_{90\%}$ = 210 °C at a SV of 3822 mL/(g h)). The Cu–Mn(1 : 6)/ZSM-5/PSSF catalyst exhibited a high stability after on-stream reaction at 260 °C for 50 h. Moreover, the zeolite membrane reactor performed better than the traditional particle fixed bed reactor. The excellent performance of the Cu–Mn(1 : 6)/ZSM-5/PSSF catalyst was associated with the presence of ZSM-5 zeolite membrane, good dispersion of the active sites, reasonable mass or heat transfer efficiency, and excellent oxygen storage ability as well as high contacting efficiency.

Huang *et al.* [69] prepared the Ni–Mn/cordierite catalysts using the wet impregnation method (Figure **23**), and investigated their toluene combustion activities. It was found that catalytic activity strongly depended on the Ni/Mn molar ratio, Ni–Mn oxides loading amount, and calcination temperature. The supported Ni–Mn oxides with a Ni/Mn molar ratio of 0.5 and Ni–Mn oxides loading amount of 10 wt% after calcination at 400 °C showed the highest activity ($T_{90\%}$ = 300 °C at a toluene concentration of 1000 ppm and a SV of 10,000 mL/(g h)), which was due to the more amount of the highly dispersed Ni–Mn oxide sites on the surface of cordierite. Working on the Fe-modified sepiolite-supported Mn–Cu mixed oxide catalysts (Cu_xMn_y/Fe-Sep, the "*x*/*y*" represents the Cu/Mn molar ratio, and *x*/*y* = 0 : 2, 1 : 0, 1 : 0.5, 1 : 2, and 1 : 4) with a Cu loading of 5 wt%, Liu *et al.* [70] claimed that catalytic activities of the Cu_xMn_y/Fe-Sep samples were higher than those of the Cu_1/Fe-Sep and Mn_2/Fe-Sep samples for ethyl acetate oxidation, and the Mn/Cu molar ratio exerted a distinct influence on activity of the sample at an ethyl acetate concentration of 2000 ppm and a SV of 20,000 mL/(g h). Among the Cu_xMn_y/Fe-Sep and Cu_1Mn_2/Sep samples, Cu_1Mn_2/Fe-Sep performed the best and showed the highest reaction rate and the lowest $T_{90\%}$ of 1.9×10^{-6} mmol/(g s) and 210 °C, respectively. Moreover, the Cu_1Mn_2/Fe-Sep sample possessed the best low-temperature reducibility and the lowest oxygen desorption temperature as well as the highest surface Mn^{4+}/Mn^{3+} or Cu^{2+}/CuO atomic ratio. The authors concluded that factors, such as the strong interaction between Cu or Mn and Fe-Sep, good low-temperature reducibility, and good chemisorbed oxygen species mobility might account for the excellent catalytic activity of Cu_1Mn_2/Fe-Sep.

After studying the low-temperature oxidation of acetone over the transition metal (M = Cu, Co, Ni, Mn or Fe)-modified ceria supported on the Al-containing MSPs (mesoporous silica particles) derived from an aerosol spray pyrolysis process (Figure **24**), Lin *et al.* [71] pointed out that among the Al-MSPs-supported Cu–Ce, Co–Ce, Ni–Ce, Mn–Ce, and Fe–Ce catalysts, Ce was the main active species in acetone oxidation, while Mn functioned as an appropriate promoter for improving the activity of Ce/Al-MSPs. It was shown that Mn amount exerted a significant influence on catalyst

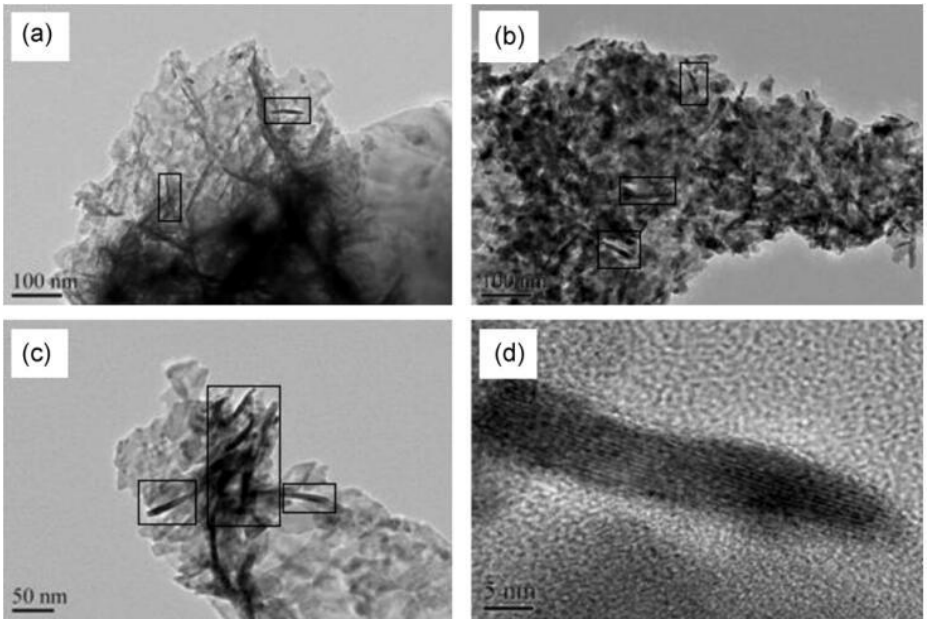

Figure 23: TEM images of the Ni–Mn/cordierite catalysts with a Ni/Mn molar ratio of 0.5 and a Ni–Mn oxides loading of 10 wt% after calcination at 400 °C [69].

Figure 24: The preparation process of the mesoporous metal/Al-MSPs composites [71].

structure, chemical state, redox behavior, and surface adsorption ability of the catalyst. The 4.4 wt% MnCe(2 : 1)/Al-MSPs catalyst exhibited the highest activity ($T_{90\%}$ = 135 °C at an acetone concentration of 1000 ppm and a SV of 15,000 mL/(g h). Furthermore, 4.4 wt% Mn–Ce(2 : 1)/Al-MSPs was remarkably stable within 55 h of on-stream reaction at 175 °C. The superior activity of 4.4 wt% MnCe(2 : 1)/Al-MSPs was attributed to the synergistic effect existing in $MnCeO_x$, which resulted in high amounts of Ce^{3+} and Mn^{4+} species, improved reducibility, and enhanced acetone adsorption ability.

Alumina, silica, zirconia, and transition metal oxides are good supports for loading the active phases (e.g., transition metal or valence-variable rare-earth oxides) in the oxidative removal of VOCs and CVOCs. For example, by adopting a wet impregnation method, Wu *et al.* [72] obtained a series of Mn_xCe_y/Al_2O_3 catalysts and evaluated their catalytic activities for the combustion of 1000 ppm CB at SV = 15,000 mL/(g h). The Mn_xCe_y/Al_2O_3 materials presented high activities for the low-temperature catalytic destruction of CB, in which 15 wt% Mn_8Ce_2/Al_2O_3 was the most active catalyst, giving a $T_{90\%}$ of 315 °C. In addition, Mn_xCe_y/Al_2O_3 with high Mn/Ce ratios were catalytically stable, which was related to their better reducibility. Wu *et al.* [73] prepared the Mn–Ce/Al_2O_3 and Mn–Ce–Mg/Al_2O_3 catalysts via a wet impregnation route, and investigated their catalytic combustion of chlorobenzene (CB). Although the 3 wt% Mn_4–Ce_1/Al_2O_3 presented a good catalytic activity for CB removal ($T_{90\%}$ = 370 °C), the 3 wt % Mn–Ce–Mg/Al_2O_3 catalyst performed the best ($T_{90\%}$ = 315 °C at a CB concentration of 1000 ppm and a SV of 15,000 mL/(g h)). Doping of Mg decreased the interaction of the Mn and Ce species with Al_2O_3, and promoted dispersion of the Mn and Ce species and formation of the Ce–Mn–O solid solution. Addition of Mg improved the redox and alkaline properties of 3 wt% Mn–Ce–Mg/Al_2O_3. Such improvements could inhibit deactivation of the catalyst since an increase in electron density at the surface decreased the adsorption of Cl that was an electron donor. Li *et al.* [74] obtained the copper and manganese-based catalysts with different supports using an impregnation method. The results indicated that the activity ($T_{90\%}$ = 229 °C) of 10 wt% CuMn(1)O_x/γ-Al_2O_3) was much higher than those of CuO_x/γ-Al_2O_3 ($T_{90\%}$ = 296 °C) and MnO_x/γ-Al_2O_3 ($T_{90\%}$ = 282 °C) for toluene oxidation at a toluene concentration of 1200 ppm and a SV of 15,000 mL/(g h), as shown in Figure **25**. The presence of water

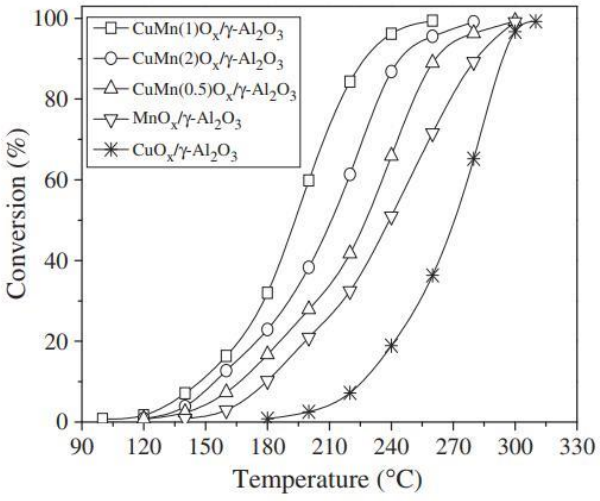

Figure 25: Toluene conversion as a function of reaction temperature over the copper/manganese-based catalysts [74].

vapor had a negative effect on catalytic activity due to the competitive adsorption of water and toluene molecules on the surface active sites. The catalytic activity drop induced by water vapor introduction decreased in the order of $CuMn(1)O_x/\gamma\text{-}Al_2O_3$ > $CuMn(1)O_x/TiO_2$ > $CuMn(1)O_x$/cordierite, which was attributed to the difference in water vapor adsorption ability of the catalysts.

Working on the $MnCuO_x/TiO_2$ catalysts synthesized by the incipient wetness impregnation method for the oxidation of CB, Vu *et al.* [75] claimed that 5 wt% $MnCuO_x/TiO_2$ was catalytically active and a total CB conversion was achieved at 350 °C at CB concentration = 500 ppm and SV = 5,000 mL/(g h). This result was attributed to formation of the spinel-type $Mn_{1.6}Cu_{1.4}O_4$ phase. At lower temperatures, however, partial deactivation occurred before a steady-state was reached. For example, CB conversion at 300 °C decreased and stabilized at 75% after 5 h of reaction, and a small amount of HCl and a trace amount of CO were detected. The reason why HCl was not detected at temperatures above 350 °C could be explained by the Deacon reaction. SEM/EDS analysis revealed the presence of chlorine uniformly dispersed on the catalyst surface. Regeneration of this catalyst in air at 350 °C allowed to recover its initial activity even though the fact that the chlorine is not completely removed from the catalyst. Using the impregnation method, Gu *et al.* [76] fabricated a series of zirconia-modified titania–alumina-supported copper–manganese oxides with a (Cu + Mn) loading of 5 wt%, and measured their catalytic activities for dichloromethane (DCM) combustion. It was observed that the 5 wt% Cu_2Mn_1/Zr–Ti–Al catalyst was very active for DCM (1200 ppm) oxidation and a complete conversion of DCM with a CO_2 selectivity of 100% was achieved at 470 °C and SV = 15,600 mL/(g h), which was attributed to the highly dispersed $CuMnO_x$ and the improved reducibility of the active phase induced by doping of Zr. The improvement in active component dispersion by adding another component is one of the meaningful approaches to generate the catalysts that are more efficient for the total oxidation of VOCs or CVOCs. Yang *et al.* [77] used the deposition–precipitation method to synthesize the $(Ce,Cr)_xO_2/MO_y$ (M = Ti, V, Nb, Mo, W or La) catalysts with the Ce and Cr contents of 36.6 and 3.4 wt%, respectively, and evaluated their catalytic activities for the total oxidation of 1,2-dichloroethane (DCE). The characterization results showed that there existed a strong metal–support interaction or synergistic effect between $(Ce,Cr)_xO_2$ and MO_y. Catalytic performance of the material was related to the nature of MO_y, crystal structure and composition, surface element distribution, and diverse redox property of $(Ce,Cr)_xO_2/MO_y$. The improved redox property and increased contents of the Ce^{3+} and Cr^{6+} species on the surface were favorable for the enhancement in activity of the catalyst. The apparent catalytic activity decreased in the sequence of in the order of $(Ce,Cr)_xO_2/Nb_2O_5$ ($T_{50\%}$ = 237 °C) > $(Ce,Cr)_xO_2/TiO_2$ ($T_{50\%}$ = 245 °C) > $(Ce,Cr)_xO_2/WO_3$ ($T_{50\%}$ = 254 °C) > $(Ce,Cr)_xO_2/MoO_3$ ($T_{50\%}$ = 264 °C) > $(Ce,Cr)_xO_2/La_2O_3$ ($T_{50\%}$ = 268 °C) > $(Ce,Cr)_xO_2/V_2O_5$ ($T_{50\%}$ = 418 °C) under the conditions of DCE concentration = 1000 ppm and SV = 9,000 mL/(g h) (Figure **26**). The $(Ce,Cr)_xO_2/Nb_2O_5$ catalyst exhibited the best activity and good durability for DCE oxidation. Moreover, the presence of water or benzene in the reaction system slightly suppressed DCE oxidation, and the catalytic activity could be recovered after cutoff of water, but slight deactivation was observed if benzene was removed away, since a small amount of coke was deposited on the catalyst surface due to the incomplete combustion of benzene.

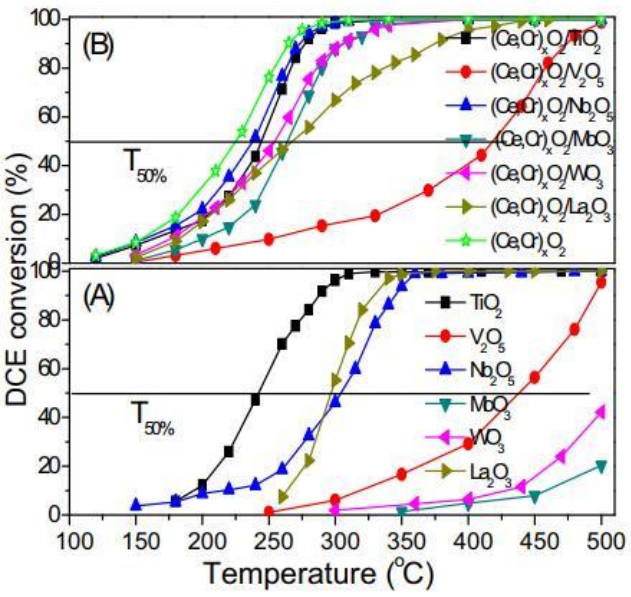

Figure 26: (**A**,**B**) DCE conversion versus reaction temperature over the different catalysts for DCE oxidation [77].

5. CONCLUSIVE REMARKS AND PERSPECTIVE

Based on the results of the above reported works, we can realize that catalytic performance was associated with one or more factors, such as specific surface area, pore structure, particle size and dispersion, adsorbed oxygen species concentration, reducibility, lattice oxygen mobility, acidity, reactant

activation ability, and/or interaction between bimetals or between metal and support of the supported noble bimetal, noble metal–transition metal, and non-precious bimetal catalysts. The stability and resistance to water, carbon dioxide or chlorine were related to the nature of the bimetal and support in the catalysts.

Although many efforts on fabrication and catalytic applications of the supported noble bimetal, noble metal–transition metal or rare earth, and non-precious bimetal catalysts in the oxidative removal of VOCs have been made, most of these catalytic materials were high in cost, which limits their wide applications in industry. Meanwhile, introduction of the second metal to a bimetallic catalyst would make surface structure of the catalyst more complicated, so it is more difficult to explore the inherent catalytic mechanisms on the surface of a bimetallic catalyst. In addition, synthesis conditions of the bimetallic catalysts should be more seriously controlled, so that they can meet the different requirements for synthesizing different bimetallic catalysts. In the future, we should pay much attention on the following aspects: (i) developing the controllable preparation strategies of novel catalysts (for example, selecting more appropriate supports and fabricating high-surface-area mesoporous materials) with high efficiency; (ii) preparing single-atom noble metal or transition metal catalysts, so that amounts of the active components can be reduced significantly and hence cost of the catalysts can be declined considerably; (iii) generating hydrophobic and sulfur-resistant catalysts, so that their moisture- and sulfur dioxide-resistance performance can be much improved; (iv) constructing core-shell-structured catalysts, so that their (hydro)thermal stability can be enhanced greatly; (v) establishing the in situ characterization techniques, so that the actual structure–performance relationships can be clarified clearly; (vi) identifying the primary reaction steps in the combustion of VOCs and CVOCs using the isotope-tracing characterization techniques and the quantum chemical calculations, so that the reaction mechanisms can be proposed reasonably; and (vii) coupling the approaches for the removal of various VOCs and CVOCs, so that the maximal removal efficiencies can be achieved.

ACKNOWLEDGEMENTS

This work is financially supported by the National Natural Science Foundation of China (21677004, 21876006, 21622701), National Natural Science Committee of China–Liaoning Provincial People's Government Joint Fund (U1908204), and Foundation on the Creative Research Team Construction Promotion Project of Beijing Municipal Institutions (IDHT20190503).

REFERENCES

[1] Deng JG, He SN, Xie SH, Yang HG, Liu YX and Dai HX. Research advancements of ordered porous metal oxide catalysts for the oxidative removal of volatile organic compounds. Chem J Chinese Univ 2014; 35: 1119-1129 (in Chinese).
http://dx.doi.org/10.7503/cjcu20131271

[2] Kamal MS, Razzak SA and Hossain MM. Catalytic oxidation of volatile organic compounds (VOCs) – A review. Atmos Environ 2016; 140: 117-134.
http://dx.doi.org/10.1016/j.atmosenv.2016.05.031

[3] Liu YX, Deng JG, Xie SH, Wang ZW and Dai HX. Catalytic removal of volatile organic compounds using ordered porous transition metal oxide and supported noble metal catalysts. Chinese J Catal 2016; 37:1193-1205.
http://dx.doi.org/10.1016/S1872-2067(16)62457-9

[4] Wang Y, Arandiyan H, Scott J, Bagheri A, Dai HX and Amal R. Recent advances in porous metal oxides for heterogeneous catalysis: a review. J Mater Chem A 2017; 5: 8825-8846.
http://dx.doi.org/10.1039/c6ta10896b

[5] Gürbüz H, Şöhret Y and Akçay H. Environmental and enviroeconomic assessment of an LPG fueled SI engine at partial load. J Environ Manage 2019; 241: 631-636.
http://10.1016/j.jenvman.2019.02.113

[6] Gürbüz H. The effect of H_2 purity on the combustion, performance, emissions and energy costs in an SI engine. Thermal Sci 2020; 24: 37-49.
http:// 10.2298/TSCI180705315G

[7] Gürbüz H and Akçay H. Experimental investigation of an improved exhaust recovery system for liquid petroleum gas fueled spark ignition engine. Thermal Sci 2015; 19: 2049-2064.
http:// 10.2298/TSCI150417181G

[8] He C, Cheng J, Zhang X, Douthwaite M, Pattisson S and Hao ZP. Recent advances in the catalytic oxidation of volatile organic compounds: A review based on pollutant sorts and sources. Chem Rev 2019; 119: 4471-4568.
https://doi.org/10.1021/acs.chemrev.8b00408

[9] Zhao XT, Xie SH, Yang HG, Deng JG and Dai HX. Catalytic removal of volatile organic compounds over porous catalysts. Global Environ Eng 2015; 2: 1-14.
http://dx.doi.org/10.15377/2410-3624.2015.02.01.1

[10] Huang HB, Xu Y, Feng QY and Leung DYC. Low temperature catalytic oxidation of volatile organic compounds: a review. Catal Sci Technol 2015; 5: 2649-2669.
http://dx.doi.org/10.1039/C4CY01733A

[11] Arandiyan H, Wang Y, Sun HY, Rezaei M and Dai HX. Ordered meso- and macroporous perovskite oxide catalysts for emerging applications. Chem Commun 2018; 54: 6484-6502.
http://dx.doi.org/10.1039/c8cc01239c

[12] Li XY, Liu YX, Deng JG, Xie SH, Zhao XT, Zhan Y, *et al.* Enhanced catalytic performance for methane combustion of 3DOM $CoFe_2O_4$ by co-loading MnO_x and Pd–Pt alloy nanoparticles. Appl Surf Sci 2017; 403: 590-600.
https://dx.doi.org/10.1016/j.apsusc.2017.01.237

[13] Persson K, Ersson A, Colussi S, Trovarelli A and Jaras SG. Catalytic combustion of methane over bimetallic Pd–Pt

catalysts: The influence of support materials. Appl Catal B: Environ 2006; 66: 175-185.

https://dx.doi.org/10.1016/j.apcatb.2006.03.010

[14] Xu P, Wu ZX, Deng JG, Liu YX, Xie SH, Guo GH, *et al.* Catalytic performance enhancement by alloying Pd with Pt on ordered mesoporous manganese oxide for methane combustion. Chinese J Catal 2017; 38: 92-105.

https://dx.doi.org/10.1016/S1872-2067(16)62567-6

[15] Amir HH, Robert EH and Natalia S. Evaluation of hydrothermal stability of encapsulated PdPt@SiO_2 catalyst for lean CH_4 combustion. Appl Catal A: Gen 2018; 556: 129-136.

https://dx.doi.org/10.1016/j.apcata.2018.02.034

[16] Tofighi G, Yu XJ, Lichtenberg H, Doronkin DE, Wang W, Wöll C, *et al.* Chemical nature of microfluidically synthesized AuPd nanoalloys supported on TiO_2. ACS Catal 2019, 9: 5462-5473.

https://dx.doi.org/10.1021/acscatal.9b00161

[17] Wang ZW, Deng JG, Liu YX, Yang HG, Xie SH, Wu ZX, *et al.* Three-dimensionally ordered macroporous $CoCr_2O_4$-supported Au–Pdalloy nanoparticles: Highly active catalysts for methane combustion. Catal Today 2017, 281: 467-476.

http://dx.doi.org/10.1016/j.cattod.2016.05.035

[18] Li XY, Liu YX, Deng JG, Zhang Y, Xie SH, Zhao XT, *et al.* 3DOM $LaMnAl_{11}O_{19}$-supported AuPd alloy nanoparticles: Highly active catalysts for methane combustion in a continuous-flow microreactor. Catal Today 2018: 308: 71-80.

http://dx.doi.org/10.1016/j.cattod.2017.07.024

[19] Xu P, Zhang X, Zhao XT, Yang J, Hou ZQ, Bai L, *et al.* Preparation, characterization, and catalytic performance of PdPt/3DOM $LaMnAl_{11}O_{19}$ for the combustion of methane. Appl Catal A: Gen 2018; 562: 284-293.

https://dx.doi.org/10.1016/j.apcata.2018.05.022

[20] Wang H, Yang W, Tian PH, Zhou J, Tang R and Wu SJ. A highly active and anti-coking Pd–Pt/SiO_2catalyst for catalytic combustion of toluene at low temperature. Appl Catal A: Gen 2017; 529: 60-67.

http://dx.doi.org/10.1016/j.apcata.2016.10.016

[21] Wu ZX, Deng JG, Xie SH, Zhao XT, Zhang KF, *et al.* Mesoporous Cr_2O_3-supported Au-Pd nanoparticles: high-performance catalysts for the oxidation of toluene. Microporous Mesoporous Mater 2016; 224: 311-322.

http://dx.doi.org/10.1016/j.micromeso.2015.11.061

[22] Wang ZW, Liu YX, Yang T, Deng JG, Xie SH and Dai HX. Catalytic performance of cobalt oxide-supported gold–palladium nanocatalysts for the removal of toluene and *o*-xylene. Chinese J Catal 2017; 38: 207-216.

https://dx.doi.org/10.1016/S1872-2067(16)62569-X

[23] Tan W, Deng JG, Xie SH, Yang HG, Jiang Y, Guo GS, *et al.* $Ce_{0.6}Zr_{0.3}Y_{0.1}O_2$ nanorod supported gold and palladium alloy nanoparticles: high-performance catalysts for toluene oxidation. Nanoscale, 2015; 7: 8510-8523.

https://dx.doi.org/10.1039/c5nr00614g

[24] Xie SH, Deng JG, Liu YX,, Zhao XT, Yang J, Zhang KF, *et al.* Effect of transition metal doping on the catalytic performance of Au–Pd/3DOM Mn_2O_3 for the oxidation of methane and *o*-xylene. Appl Catal B Environ 2017; 206; 221-232.

http://dx.doi.org/10.1016/j.apcatb.2017.01.030

[25] Yang J, Liu YX, Deng JG, Zhao XT, Zhang KF, Han Z, *et al.* AgAuPd/meso-Co_3O_4: High-performance catalysts for methanol oxidation. Chinese J Catal 2019; 40: 837-848.

https://dx.doi.org/10.1016/S1872-2067(18)63205-X

[26] Saint-Lager MC, Languille MA, Cadete Santos Aires FJ, Bailly A, Garaudée S, Ehret E, *et al.* Carbon monoxide oxidation promoted by a highly active strained PdO layer at the surface of $Au_{30}Pd_{70}$(110). ACS Catal 2019; 9; 4448-4461.

https://dx.doi.org/10.1021/acscatal.8b04190

[27] Wang Y, Arandiyan H, Scott J, Akia M, Dai HX, Deng JG, *et al.* High performance Au−Pd supported on 3D hybrid strontium-substituted lanthanum manganite perovskite catalyst for methane combustion. ACS Catal 2016; 6: 6935-6947.

https://dx.doi.org/10.1021/acscatal.6b01685

[28] Wang Y, Dai CY, Chen BB, Wang YD, Shi C and Guo XW. Nanoscale HZSM-5 supported PtAg bimetallic catalysts for simultaneous removal of formaldehyde and benzene. Catal Today 2015; 258: 616-626.

http://dx.doi.org/10.1016/j.cattod.2015.03.042

[29] Abbott HL, Aumer A, Lei Y, Asokan C, Meyer RJ, Sterrer M, *et al.* CO adsorption on monometallic and bimetallic Au–Pd nanoparticles supported on oxide thin films. J Phys Chem C 2010; 114: 17099-17104.

https://dx.doi.org/10.1021/jp1038333

[30] Jiang L, Yang N, Zhu JQ and Song CY. Preparation of monolithic Pt–Pd bimetallic catalyst and its performance in catalytic combustion of benzene series. Catal Today 2013; 216: 71-75.

http://dx.doi.org/10.1016/j.cattod.2013.05.026

[31] Amir HH, Natalia S and Robert EH. Kinetics of low-temperature methane oxidation over SiO_2-encapsulated bimetallic Pd−Pt nanoparticles. Ind Eng Chem Res 2018; 57: 8160-8171.

http://dx.doi.org/10.1021/acs.iecr.8b01338

[32] Xie SH, Deng JG, Liu YX, Zhang ZH, Yang HG, Jiang Y, *et al.* Excellent catalytic performance, thermal stability, and water resistance of 3DOM Mn_2O_3-supported Au–Pd alloy nanoparticles forthe complete oxidation of toluene. Appl Catal A: Gen 2015; 507: 82-90.

http://dx.doi.org/10.1016/j.apcata.2015.09.026

[33] Xie SH, Deng JG, Zang SM, Yang HG, Guo GS, Arandiyan H, *et al.* Au–Pd/3DOM Co_3O_4: Highly active and stable nanocatalysts for toluene oxidation. J Catal 2015; 322: 38-48.

http://dx.doi.org/10.1016/j.jcat.2014.09.024

[34] Zhang X, Liu YX, Deng JG, Yu XH, Han Z, Zhang KF, *et al.* Alloying of gold with palladium: An effective strategy to improve catalytic stability and chlorine-tolerance of the 3DOM CeO_2-supported catalysts in trichloroethylene combustion. Appl Catal B: Environ 2019; 257: 117879.

https://dx.doi.org/10.1016/j.apcatb.2019.117879

[35] Bonelli R, Albonetti S, Morandi V, Ortolani L, Riccobene PM, Scirè S, *et al.* Design of nano-sized FeO_x and Au/FeO_x catalysts supported on CeO_2 for total oxidation of VOC. Appl Catal A: Gen 2011; 395: 10-18.

http://dx.doi.org/10.1016/j.apcata.2011.01.017

[36] Qian K, Fang J, Huang WX, He B, Jiang ZQ, Ma YS, *et al.* Understanding the deposition–precipitation process for the preparation of supported Au catalysts. J Mol Catal A: Chem 2010; 320: 97-105.

http://dx.doi.org/10.1016/j.molcata.2010.01.010

[37] Solsona B, Pérez-Cabero M, Vázquez I, Dejoz A, García T, Álvarez-Rodríguez J, *et al.* Total oxidation of VOCs on Au nanoparticles anchored on Co doped mesoporous UVM-7 silica. Chem Eng J 2012; 187: 391-400.

http://dx.doi.org/10.1016/j.cej.2012.01.132

[38] Grisel RJH and Nieuwenhuys BE. A comparative study of the oxidation of CO and CH_4 over Au/MO_x/Al_2O_3 catalysts. Catal Today 2001; 64: 69-81.

http://dx.doi.org/10.1016/s0920-5861(00)00510-1

[39] Yang HG, Deng JG, Xie SH, Jiang Y, Dai HX and Au CT. Au/MnO_x/3DOM SiO_2: Highly active catalysts for toluene oxidation. Appl Catal A: Gen 2015; 507: 139-148.

http://dx.doi.org/10.1016/j.apcata.2015.09.043

[40] Jiang Y, Xie SH, Yang HG, Deng JG, Liu YX and Dai HX. Mn_3O_4–Au/3DOM $La_{0.6}Sr_{0.4}CoO_3$: High-performance catalysts for toluene oxidation. Catal Today 2017; 281: 437-446.

http://dx.doi.org/10.1016/j.cattod.2016.05.012

[41] Monai M, Montini T, Chen C, Fonda E, Gorte RJ and Fornasiero P. Methane catalytic combustion over hierarchical Pd@CeO_2/Si–Al_2O_3: Effect of the presence of water. ChemCatChem 2015; 14: 2038-2046.

http://dx.doi.org/10.1002/cctc.201402717

[42] Chen C, Yeh YH, Cargnello M, Murray CB, Fornasiero P and Gorte RJ. Methane oxidation on Pd@ZrO_2/Si–Al_2O_3 is enhanced by surface reduction of ZrO_2. ACS Catal 2014; 4: 3902-3909.

http://dx.doi.org/10.1021/cs501146u

[43] Satsuma A, Tojo T, Okuda K, Yamamoto Y, Arai S and Oyama J. Effect of preparation method of Co-promoted Pd/alumina for methane combustion. Catal Today 2015; 242: 308-314.

http://dx.doi.org/10.1016/j.cattod.2014.05.046

[44] Zuo SF and Qi CZ. Modification of Co/Al_2O_3 with Pd and Ce and their effects on benzene oxidation. Catal Commun 2011; 15: 74-77.

http://dx.doi.org/10.1016/j.catcom.2011.08.021

[45] Xie SH, Liu YX, Deng JG, Zhao XT, Yang J, Zhang KF, *et al.* Three-dimensionally ordered macroporous CeO_2-supported Pd@Co nanoparticles: Highly active catalysts for methane oxidation. J Catal 2016; 342: 17-26.

http://dx.doi.org/10.1016/j.jcat.2016.07.003

[46] Hou ZQ, Liu YX, Deng JG, Lu Y, Xie SH, Fang XZ, *et al.* Highly active and stable Pd–GaO_x/Al_2O_3 catalysts derived from intermetallic Pd_5Ga_3 nanocrystals for methane combustion. ChemCatChem 2018; 24: 5637-5648.

http://dx.doi.org/10.1002/cctc.201801684

[47] Widjaja H, Sekizawa K, Eguchi K and Arai H. Oxidation of methane over Pd/mixed oxides for catalytic combustion. Catal Today 1999; 47: 95-101.

http://dx.doi.org/10.1016/s0920-5861(98)00286-7

[48] Zou XL, Rui Z.B, Song SQ and Ji HB. Enhanced methane combustion performance over $NiAl_2O_4$-interface promoted Pd/γ-Al_2O_3. J Catal 2016; 338: 192-201.

http://dx.doi.org/10.1016/j.jcat.2015.12.031

[49] Ferreira RSG, de Oliveira PGP and Noronha FB. Characterization and catalytic activity of Pd/V_2O_5/Al_2O_3 catalysts on benzene total oxidation. Appl Catal B: Environ 2004; 50: 243-249.

http://dx.doi.org/10.1016/j.apcatb.2004.01.006

[50] Xie SH, Liu YX, Deng JG, Zang SM, Zhang ZH, Arandiyan H, *et al.* Efficient removal of methane over cobalt-monoxide-doped AuPd nanocatalysts. Environ Sci Technol 2017; 51: 2271-2279.

http://dx.doi.org/10.1021/acs.est.6b03983

[51] Sedjame HJ, Fontaine C, Lafaye G, and Barbier J. On the promoting effect of the addition of ceria to platinum based alumina catalysts for VOCs oxidation. Appl Catal B: Environ 2014; 144: 233-242.

http://dx.doi.org/10.1016/j.apcatb.2013.07.022

[52] Nobuhito I, Jeong M, Nunotani N and Moriyama N. Introduction of NiO in Pt/CeO_2–ZrO_2/γ-Al_2O_3 catalysts for removing toluene in indoor air. Mate Lett 2017; 208: 43-45.

http://dx.doi.org/10.1016/j.matlet.2017.05.048

[53] Jiang ZY, Feng XB, Deng JL, He C, Douthwaite M, Yu Y, *et al.* Atomic-scale insights into the low-temperature oxidation of methanol over a single-atom Pt_1–Co_3O_4 catalyst. Adv Funct Mater 2019; 29: 1902041.

http://dx.doi.org/10.1002/adfm.201902041

[54] Rintramee K, Föttinger K, Rupprechter G and Wittayakuna J. Ethanol adsorption and oxidation on bimetallic catalysts containing platinum and base metal oxide supported on MCM-4. Appl Catal B: Environ 2012; 115-116: 225-235.

http://dx.doi.org/10.1016/j.apcatb.2011.11.050

[55] Yang HG, Deng JG, Liu YX, Xie SH, Xu P and Dai HX. Pt/Co_3O_4/3DOM Al_2O_3: Highly effective catalysts for toluene combustion. Chinese J Catal 2016; 37: 934-946.

http://dx.doi.org/10.1016/S1872-2067(15)61095-6

[56] He C, Jiang ZY, Ma MD, Zhang XD, Douthwaite M, Shi JW, *et al.* Understanding the promotional effect of Mn_2O_3 on micro-/mesoporous hybrid silica nanocubic-supported Pt catalysts for the low-temperature destruction of methyl ethyl ketone: an experimental and theoretical study. ACS Catal 2018; 8: 4213-4229.

http://dx.doi.org/10.1021/acscatal.7b04461

[57] Hou ZY, Zhou XY, Lin T, Chen YQ, Lai XX, Feng J, *et al.* The promotion effect of tungsten on monolith Pt/$Ce_{0.65}Zr_{0.35}O_2$ catalysts for the catalytic oxidation of toluene. New J Chem 2019; 43: 5719-5726.

http://dx.doi.org/10.1039/c8nj06245e

[58] Huang QQ, Xue XM and Zhou RX. Catalytic behavior and durability of CeO_2 or/and CuO modified USY zeolite catalysts for decomposition of chlorinated volatile organic compounds. J Mol Catal A: Chem 2011; 344: 74-82.

http://dx.doi.org/10.1016/j.molcata.2011.04.021

[59] Huang QQ, Meng ZH and Zhou RX. The effect of synergy between Cr_2O_3–CeO_2 and USY zeolite on the catalytic performance and durability of chromium and cerium modified USY catalysts for decomposition of chlorinated volatile organic compounds. Appl Catal B: Environ 2012; 115-116: 179-189.

http://dx.doi.org/10.1016/j.apcatb.2011.12.028

[60] Abdullah AZ, Bakar MZA and Bhatia S. Combustion of chlorinated volatile organic compounds (VOCs) using bimetallic chromium-copper supported on modified H-ZSM-5 catalyst. J Hazard Mater 2006; 129: 39-49.

http://dx.doi.org/10.1016/j.jhazmat.2005.05.051

[61] Yang P, Shi ZN, Tao F, Yang SS and Zhou RX. Synergistic performance between oxidizability and acidity/texture properties for 1,2-dichloroethane oxidation over $(Ce,Cr)_xO_2$/zeolite catalysts. Chem Eng Sci 2015; 134: 340-347.

http://dx.doi.org/10.1016/j.ces.2015.05.024

[62] Huang QQ, Zuo SF and Zhou RX. Catalytic performance of pillared interlayered clays (PILCs) supported CrCe catalysts for deep oxidation of nitrogen-containing VOCs. Appl Catal B: Environ 2010; 95: 327-334.

http://dx.doi.org/10.1016/j.apcatb.2010.01.011

[63] Feng BB, Wei YX, Qiu YN, Zuo SF and Ye N. Ce-modified AlZr pillared clays supported-transition metals for catalytic combustion of chlorobenzene. J Rare Earth 2018; 36: 1169-1174.

http://dx.doi.org/10.1016/j.jre.2018.03.026

[64] Zuo SF, Ding ML, Tong J, Feng LC and Qi CZ. Study on the preparation and characterization of a titanium-pillared clay-supported CrCe catalyst and its application to the degradation of a low concentration of chlorobenzene. Appl Clay Sci 2015; 105-106: 118-123.

http://dx.doi.org/10.1016/j.clay.2014.12.033

[65] Kan JW, Deng L, Li B, Huang Q, Zhu SM, Shen SB and Chen YW. Performance of co-doped Mn-Ce catalysts supported on cordierite for low concentration chlorobenzene oxidation. Appl Catal A: Gen 2017; 530: 21-29.
http://dx.doi.org/10.1016/j.apcata.2016.11.013

[66] Yang P, Xue XM, Meng ZH and Zhou RX. Enhanced catalytic activity and stability of Ce doping on Cr supported HZSM-5 catalysts for deep oxidation of chlorinated volatile organic compounds. Chem Eng J 2013; 234: 203-210.
http://dx.doi.org/10.1016/j.cej.2013.08.107

[67] Sun PF, Wang WL, Dai XX, Weng XL and Wu ZB. Mechanism study on catalytic oxidation of chlorobenzene over $Mn_xCe_{1-x}O_2$/H-ZSM5 catalysts under dry and humid conditions. Appl Catal B: Environ 2016; 198: 389-397.
http://dx.doi.org/10.1016/j.apcatb.2016.05.076

[68] Chen HH, Zhang HP and Yan Y. Fabrication of porous copper/manganese binary oxides modified ZSM-5 membrane catalyst and potential application in the removal of VOCs. Chem Eng J 2014; 254: 133-142.
http://dx.doi.org/10.1016/j.cej.2014.05.083

[69] Huang Q, Zhang ZY, Ma WJ, Chen YW, Zhu SM and Shen SB. A novel catalyst of Ni–Mn complex oxides supported on cordierite for catalytic oxidation of toluene at low temperature. J Ind Eng Chem 2012; 18: 757-762.
http://dx.doi.org/10.1016/j.jiec.2011.11.129

[70] Liu LS, Song Y, Fu ZD, Ye Q, Cheng SY, Kang TF and Dai HX. Enhanced catalytic performance of Cu- and/or Mn-loaded Fe-Sep catalysts for the oxidation of CO and ethyl acetate. Chinese J Chem Eng 2017; 25: 1427-1434.
http://dx.doi.org/10.1016/j.cjche.2017.01.005

[71] Lin LY and Bai HL. Promotional effects of manganese on the structure and activity of Ce–Al–Si based catalysts for low-temperature oxidation of acetone. Chem Eng J 2016; 291: 94-105.
http://dx.doi.org/10.1016/j.cej.2016.01.098

[72] Wu M, Wang XY, Dai QG, Gu YX and Li D. Low temperature catalytic combustion of chlorobenzene over Mn–Ce–O/γ-Al_2O_3 mixed oxides catalyst. Catal Today 2010; 158: 336-342.
http://dx.doi.org/10.1016/j.cattod.2010.04.006

[73] Wu M, Wang XY, Dai QG and Li D. Catalytic combustion of chlorobenzene over Mn–Ce/Al_2O_3 catalyst promoted by Mg. Catal Commun 2010; 11: 1022-1025.
http://dx.doi.org/10.1016/j.catcom.2010.04.011

[74] Li X, Wang LJ, Xia QB, Liu ZM and Li Z. Catalytic oxidation of toluene over copper and manganese-based catalysts: Effect of water vapor. Catal Commun 2011; 14: 15-19.
http://dx.doi.org/10.1016/j.catcom.2011.07.003

[75] Vu VH, Belkouch J, Ould-Dris A and Taouk B. Removal of hazardous chlorinated VOCs over Mn–Cu mixed oxide-based catalyst. J Hazard Mater 2009; 169: 758-765.
http://dx.doi.org/10.1016/j.jhazmat.2009.04.010

[76] Gu YL, Yang YX, Qiu YM, Sun KP and Xu XL. Combustion of dichloromethane using copper–manganese oxides supported on zirconium modified titanium-aluminum catalysts. Catal Commun 2010; 12: 277-281.
http://dx.doi.org/10.1016/j.catcom.2010.10.006

[77] Yang P, Zuo SF, Shi ZN, Tao F and Zhou RX. Elimination of 1,2-dichloroethane over $(Ce,Cr)_xO_2/MO_y$ catalysts (M = Ti, V, Nb, Mo, W and La). Appl Catal B: Environ 2016; 191: 53-61.
http://dx.doi.org/10.1016/j.apcatb.2016.03.017

Received on 23-05-2020 Accepted on 10-06-2020 Published on 16-07-2020

DOI: https://doi.org/10.15377/2410-3624.2020.07.1